QUANTITATIVE CHARACTERIZATION OF POLYMER SCRATCH BEHAVIOR USING A STANDARDIZED SCRATCH TEST

A Thesis

by

ROBERT LEE BROWNING

Submitted to the Office of Graduate Studies of
Texas A&M University
in partial fulfillment of the requirements for the degree of

MASTER OF SCIENCE

May 2006

Major Subject: Mechanical Engineering

QUANTITATIVE CHARACTERIZATION OF POLYMER SCRATCH BEHAVIOR USING A STANDARDIZED SCRATCH TEST

A Thesis

by

ROBERT LEE BROWNING

Submitted to the Office of Graduate Studies of
Texas A&M University
in partial fulfillment of the requirements for the degree of

MASTER OF SCIENCE

Approved by:

Chair of Committee,	Hung-Jue Sue
Committee Members,	Jaime Grunlan
	David Bergbreiter
Head of Department,	Dennis O'Neal

May 2006

Major Subject: Mechanical Engineering

ABSTRACT

Quantitative Characterization of Polymer Scratch Behavior Using a Standardized Scratch Test. (May 2006)

Robert Lee Browning, B.S., Texas A&M University

Chair of Advisory Committee: Dr. Hung-Jue Sue

The lack of a widely-accepted quantitative methodology for evaluating the scratch behavior of polymeric materials has resulted in the development and establishment of a new methodology recently standardized as ASTM D7027-05. Using a custom-built instrumented scratch machine, it is possible to produce controlled, repeatable scratches on polymer surfaces under constant or linearly increasing loading conditions at constant or increasing scratch rates. Software-aided digital image analysis along with material science tools (SEM, OM, FTIR, etc.) allows polymer scratch behavior to be analyzed without the ambiguity inherent in the past.

The current work will serve to describe the motivation for the development of this methodology as well as illustrate the effectiveness of the increasing load/constant rate test mode in three case studies. First, it will be shown that an acrylic coating on a steel system exhibits three zones of scratch damage: adhesive delamination, transverse cracking and finally buckling failure. It will be discussed how increases in ductility and thickness serve to improve the scratch resistantance of this coating/substrate system. Improvements in the scratch behavior of thermoplastic olefins (TPOs) through the use of

surface-treated talc fillers and the slip agent erucamide will be shown in the second case. It was found that the surface-treatment of the talc likely allows for enhanced migration of the erucamide to the TPO surface, thus lowering the surface friction and greatly increasing scratch resistance. Finally, the effects of processing conditions, namely injection molding, on the scratch behavior of neat *i*-polypropylene will be represented by the results of scratch tests conducted where the scratch direction was oriented both along and transverse to the polymer melt flow direction. Based on the findings of the study, there appears to be a high degree of surface anisotropy introduced to injection-molded polymers due to complex fluid flow regimes as well as non-uniform cooling properties.

ACKNOWLEDGEMENTS

First and foremost, I would like to extend great thanks and gratitude to my committee chair, Professor Hung-Jue Sue, without whose patience and wisdom this degree never would have been attained. Thanks are also due to Professors Jaime Grunlan and David Bergbreiter for their interest in and support of this research.

Allan Moyse is praised for his paramount role in making this research possible. Appreciation goes to Doctor Goy Teck Lim for his mentorship and kind advice. The staff of the Microscopy and Imaging Center is recognized for their undying support and invaluable knowledge. Credit is given to the members of the Texas A&M Polymer Scratch Behavior Consortium and the Society of Plastics Engineers for financial support. Thank you also to the faculty and staff of the Department of Mechanical Engineering for making this research effort an enjoyable experience.

Last, but in no way least, I would like to express sincere thanks to the members of my family (Dad, Meme, Pawpaw and Kim), Ms. Markey Ford Weaver and my good friends who have supported me through thick and thin and have led me down the path to a bright future. As Meme would say, here's hoping that you all live forever and that I never die.

TABLE OF CONTENTS

CHAPTER Page

LIST OF FIGURES

FIGURE Page

FIGURE Page

LIST OF TABLES

CHAPTER I

INTRODUCTION

The majority of materials integrated into consumer products in recent years has been largely comprised of polymers. When certain properties of polymeric materials are compared to those of metals and ceramics, it becomes clear why polymers are implemented to do a job where one of the other classes of materials would previously have been used. Polymers are relatively cheaper to process and manufacture, recycle easily, are more lightweight and resistant to corrosion and can be rapidly fabricated into complex parts with little effort. These benefits have drawn considerable attention from industry and have led to the development of strong products that can withstand the rigors of consumption.

To illustrate, the automotive industry saw the positive aspects of making interior and exterior car parts from polymeric materials. These parts can be made inexpensively from materials such as polypropylene (PP). A plastic bumper will be easier and cheaper to repair or replace than a metal one that has been dented or corroded. In addition, the low density of polymers will ultimately make the car lighter and more aerodynamic. Therefore, the automotive industry has set its sights on employing as much polymeric material into the manufacture of an automobile as possible.

Sometimes, however, an amalgam of different materials is required for certain applications. In the case of metal piping systems that are buried in the presence of

---

This thesis follows the style of the journal of Polymer Engineering and Science.

moisture, water-resistant polymer coatings are applied to the pipes as a rust barrier. Polymer coatings can also be used to block, and sometimes conduct, electricity and oxygen. Paints are a type of polymeric coating that can provide protection for the substrate while simultaneously giving the visible surface a more appealing finish or texture. These polymer coatings provide protection for materials ideal for a particular application that would otherwise not be able to survive in the prescribed environment. In certain instances, a tradeoff exists between certain properties when using polymers. While one property shows outstanding behavior, another one may suffer. In this case, fillers or additives can be added to the matrix or the chemical makeup of the polymer can be altered in order to achieve the desired performance.

Regardless of the material, whether metal, polymer or ceramic, the materials that make up the products must be tested under many conditions to show that they meet the requirements of the application in order to provide consumers with reliable products. Tensile tests show how much stress and strain the material can withstand under an applied load before it fails. Impact tests provide information on crack propagation and tear strength when the material is hit by a sudden applied force. In a scratch test, surface friction behavior as well as visibility can be characterized by applying controlled scratches to the surface of materials.

To eliminate subjectivity and ambiguity, once a test method has been reviewed and deemed acceptable by the American Society for the Testing of Materials (ASTM), it is designated as a standard testing methodology. These standards dictate the appropriate means for testing materials under prescribed conditions. Many of the ASTM standards

already in place for metals and ceramics yield good quality data. However, it has been more of a challenge to establish such standards for polymers.

Polymers, quite different from metals and ceramics, possess an extremely complex molecular structure. This makes it nearly impossible to draw parallels from the data analysis methods that go along with the tests employed for metals and ceramics which, relatively, have a much simpler molecular makeup. To emphasize this point, consider a tensile stress/strain curve for a metal or a ceramic. The resulting plot of stress as a function of strain would be somewhat linear with a positive slope. In contrast, a stress/strain curve for a polymer will exhibit similar linear behavior at first, but will also contain distinct segments of differing slope which give information regarding mechanical phenomena unique to polymers. Hence, it becomes necessary to develop effective and objective test methods that can accommodate this inherent complexity.

The scratch test has been gaining more and more credibility in polymer applications as research has continued over the years. Even though advances have been made in technological design of the testing device, the main problem has been eliminating, or at least minimizing, the subjectivity that goes along with characterizing a scratch. When addressing scratch resistance, there are two main areas of focus: aesthetics and protection. The former is important to applications such as paint, glosscoats or surfaces that will be devalued by blemishes, scuffs, mars or gouges. The latter is relatively self-explanatory in that the surface must be kept free of scratches than can damage either delicate parts on the surface, like a microchip, or the surface beneath a coating, like the underground pipe application stated before.

Many test methods have been developed for assessing scratch damage in polymer bulks and coating materials. The designs of these apparatus are often based on modifying instruments that already have other purposes. A nanoindenter or an atomic force microscope can be modified to take advantage of the small tip on the instrument to make scratches. The scratches made by these modified setups are generally on the microscale, generating around 1 microNewton of normal load or below, and can prove quite valuable for small-scale evaluation. This is not suitable for industrial tests, however, as the applied normal load is often required to be orders of magnitude larger.

For these applications, the scratch test currently accepted and used by the automotive industry employs the use of the Taber® Multi-Finger Scratch/Mar Tester (Figure 1). This methodology is used at such companies as Ford (Test #BN 108-13), General Motors (Test #GMN3943) and Daimler-Chrysler (Test #LP-463DD-18-01). Often dubbed the "five-finger" scratch test, this method uses five pneumatically-driven deadweight-loaded styluses to produce up to five controlled scratches on the surface of materials. The five scratches are then compared qualitatively or using light-scattering methods. Since deadweights of fixed, finite value are used for load application, the load at which the failure criterion is met might be interpolated or reported as a range.

Observing the potential to build upon the foundation set up by the five-finger scratch test, a methodology for quantitatively and objectively characterizing the scratch behavior of polymers was developed at Texas A&M University using an instrumented, custom-designed scratch machine. As a result, the method was reviewed and standardized by ASTM in 2005 under designation D 7027-05 [1]. The testing apparatus

(PTC Scratch Machine III, referred to as Scratcher III for brevity) was designed, fabricated and constructed at Texas A&M University.

FIG 1. The Taber® Multi-Finger Scratch/Mar Tester.

The components of the Scratcher III are shown in Figure 2. The Testing Apparatus (Figure 2a) is controlled by two servo motors. One servo motor operates the hydraulic cylinder/pneumatic diaphragm combination for load application and vertical tip translation. The other servo motor indirectly provides horizontal translation for the scratch tip. Sensors are equipped to capture *in-situ* normal and tangential load and horizontal and vertical scratch tip displacement. The Power Supply (Figure 2b) houses all necessary electronic components for operation of the Scratcher III. Test execution and data capture are achieved by using LabVIEW (National Instruments, Inc.), a software-based user interface program installed on the PC User Interface and Analysis System (Figure 2c).

The methodology requires the input of four parameters: scratch speed, initial load, final load and scratch length. ASTM D7207-05 dictates that a standard scratch will be conducted at a constant or increasing speed in the range of 0-100 mm/s for a scratch

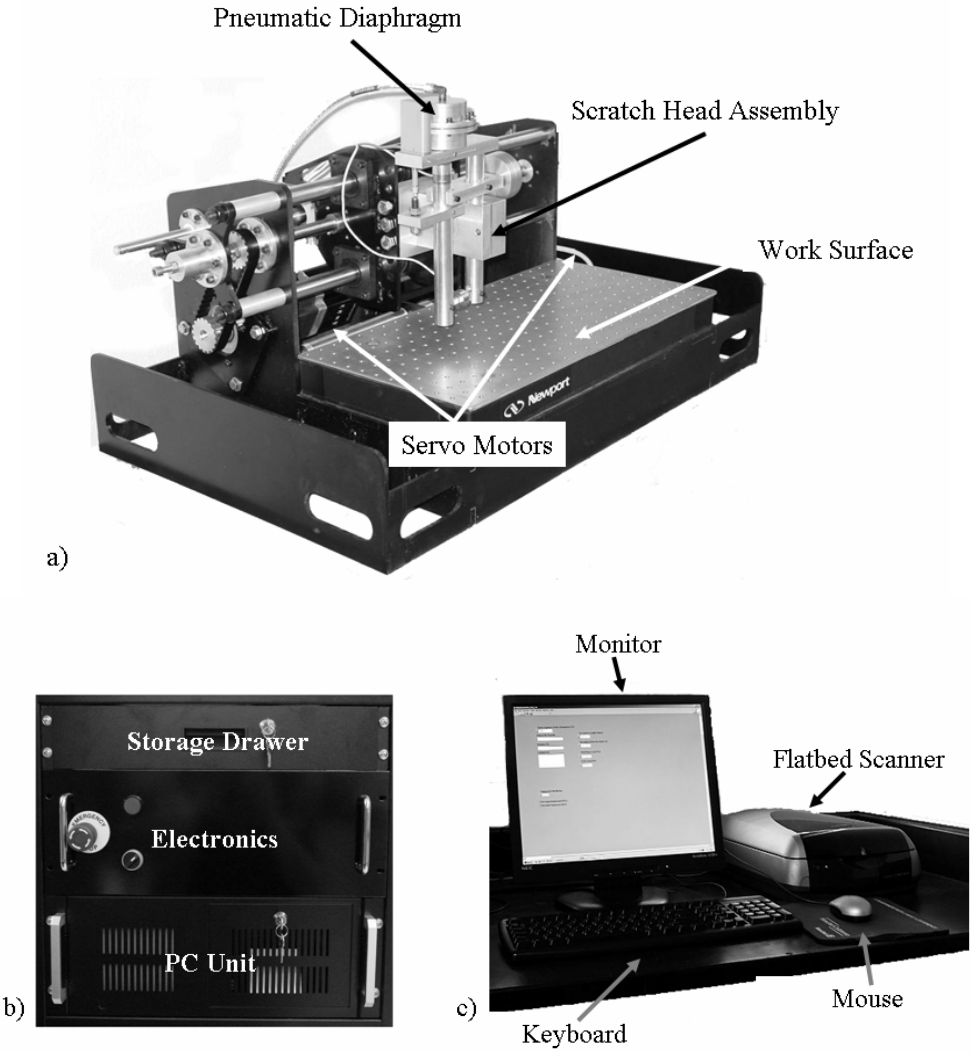

FIG 2. The PTC Scratch Machine III is composed of a) the testing apparatus, b) the power supply and c) the PC user interface and analysis system.

length of 100 mm over a constant or linearly increasing load range within 1-50 N. A spherical tip was designated as the standard tip geometry, but a variety of tip geometries and materials can be interchanged based on the application and properties of the polymer. In most cases, the increasing load scratch test can provide the most useful information regarding polymer scratch behavior.

Scratch Visibility Evaluation

Since load and distance both increase in a linear fashion, the load at a particular point in a scratch can be trivially calculated by using the following equation:

$$F_z = \left(\frac{x}{L}\right)\left(F_f - F_0\right) + F_0 \tag{1}$$

where F_z (N) is the normal load at point x, x is the point of interest (mm) and F_f and F_0 are the final and initial load, respectively. In this fashion, the critical load where certain damage features or transitions occur can be easily extracted.

One such feature of interest is the onset of scratch visibility. This is arguably the most subjective part of evaluating scratch damage. Human observers will perceive a scratch as "bad" or "severe" based on different personal biases. There have been several studies that have attempted to approach this problem. Hutchings et al. [2] conducted an extensive study using human observers to rate the severity of scratch damage on polymeric surfaces. Though the results obtained from human subjects showed good correlation with their independent image analysis on the difference in gray-scale levels

between damaged and undamaged areas, the subjectivity of human observation cannot be disregarded.

In contrast, Rangarajan et al. recently introduced the more objective concept of light scattering as a method to quantitatively address scratch visibility [3]. Their method uses a combination of uniform lighting and a telecentric lens/camera setup at different angles to measure light scattering relative to the undamaged surface resulting from surface gloss and roughness. Kody and Martin also proposed a digital image analysis method in which they measured the differences in the level of scattered light in the damaged region to quantify scratch damage [4].

The latter methods take into account that scratch visibility is caused by the scattering of light by damage features such as crazes, microvoids or rough material deformation. Through the work in this study, it was found that scanning the scratched polymer surfaces with a PC scanner and post-processing using image analysis software proved to be an effective way to eliminate ambiguity in determining when a scratch becomes visible.

Specifically, the specimen is scanned in grayscale mode at 3200x3200 dpi resolution with an EPSON 4870 Perfection Photo flatbed PC scanner. The resulting image is then opened in ImageJ, a software-based digital image analysis program. Using the grayscale threshold option, the pixels making up the image can be assigned a contrasting color based on their “gray level”. In this way, the portion of the polymer that scatters the most light, and thus exhibits scratch visibility, can be excluded from the rest of the surface. The distance to the onset point can be easily measured and the load at

which this occurs, termed the critical load for the onset of scratch visibility, can be calculated using Equation 1.

Frictional Behavior

The scratching coefficient of friction (SCOF) is defined as the ratio of the tangential force to the normal force as defined in Figure 3. Plotting this curve as a function of scratch length provides insight to many aspects of the material. This curve can give a good representation as to the roughness of the scratch as well as how easily the material can be displaced. The tangential force is largely what influences the behavior of this curve. In this light, sudden changes in the behavior of the curve could be related to a sudden increase or decrease in tangential force which could be indicative of transitions in the scratch damage mechanisms. The verification of this behavior with scanning electron microscopy (SEM) or optical microscopy (OM) yields yet another quantitative means of addressing scratch resistance.

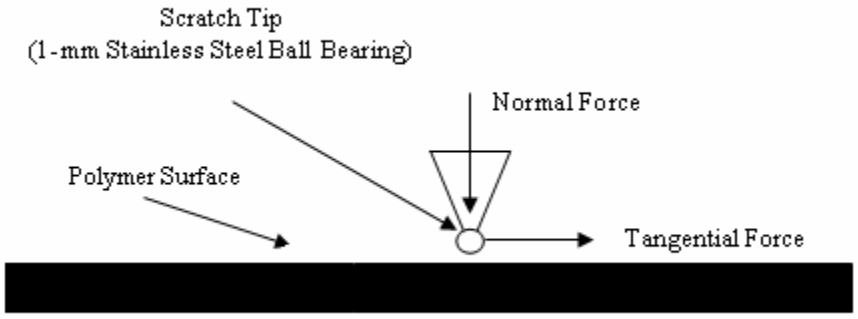

FIG 3. Definition of forces used to calculate the scratching coefficient of friction (SCOF).

Scratch Hardness

In the past, evaluating the hardness of materials was a relative matter. The Mohs hardness scale was developed by rubbing various minerals together. The mineral that damaged the other was deemed the harder material. The Mohs scale ranges from a hardness of 1 (softest) corresponding to talc to 10 (hardest) corresponding to diamond. As research became more sophisticated, a different definition of material hardness was adopted. According to the new definition, the hardness of a material is dependent upon the extent of penetration of an indenter under an applied normal load. The indentation hardness was given by Briscoe [5] as the applied normal load divided by the projected contact area and is highly dependent on the geometry of the indenter.

Using this concept, an additional parameter was adopted for polymer scratch behavior. The scratch hardness is defined analogous to the indentation hardness as the normal load (F_z) divided by the contact area, which for a spherical indenter is the area of a circle with the scratch width (w) as its diameter:

$$Ac = \frac{\pi w^2}{4} \tag{2}$$

$$H_S = \frac{F_z}{A_c} = \frac{4qF_z}{\pi w^2} \tag{3}$$

The variable q is a parameter that corresponds to the recoverability of the polymer. For the work herein, full recovery is assumed and q is therefore taken to be equal to 1. The applied normal force (N) is plotted against corresponding measured values of contact area (mm^2). If the linear regression fit line of the resulting data points is reasonably linear (e.g. $R^2 \approx 0.95$), this slope represents the scratch hardness of the material in MPa.

If the trendline behaves nonlinearly, this could indicate that the surface of the material is of a layered nature or, again, that a transition in the damage mechanism has occurred.

It will be shown in the following chapters that the combination of this testing and analysis methodology along with applied material science analysis can prevail over the shortcomings of the existing methods and will also show its inherent versatility.

CHAPTER II

EFFECT OF DUCTILITY AND THICKNESS ON THE SCRATCH BEHAVIOR OF POLYMER COATINGS

Coatings provide many important functions for tools, consumer goods, pipelines, industrial equipment, etc. Tungsten carbide as well as other inorganic materials is regularly used to coat the surface of metal parts and tools to improve properties such as surface hardness, friction and wear resistance, and service lifetime. Thin polymer coatings have been explored as possibilities for many protective and aesthetic applications including automotive gloss-coats, flooring varnish, paint systems, adhesion-promoting primers, and scratch-resistance improvement of optical lenses [6-12]. Seeing as how polymeric coatings serve the purpose of improving or protecting the surface of materials, it is obligatory to learn how to improve the coating resistance to scratch damage.

In general, the coating scratch damage mechanisms involve elastic and plastic deformation, cracking, chipping, delamination, etc. Many industrial test methods exist to evaluate coating resistance against scratch damage. For example, the knife test (ASTM D 6677) [13] involves an operator using a knife to "chip away" the coating, qualitatively and comparatively evaluating which coating shows the best resistance against chipping or cutting. The tape test (ASTM D 3359) [14], sometimes referred to as the peel test, uses a strip of pressure-sensitive adhesive tape applied over a pattern cut into the surface of the coating. The tape is then removed in a controlled manner and the

operator records the extent of failure or delamination. The pencil hardness test (ASTM D 3363) [15] is similar in principle to the Mohs hardness test for minerals. Several pencils with varying lead hardness values are used to apply pressure with the lead to the coating surface. The lead hardness that produces damage to the coating is recorded as the coating's pencil hardness.

There are still other standard evaluation methods [16-18]. But upon review, their deficiencies become readily evident. Many of these test methods depend on the competency of the operator and on oversimplification of the complex material response in polymeric coatings systems. In recent years, scratch testing has become a more popular and meaningful way to address coating damage. The new scratch test methodology developed using the Scratcher III has been shown to be effective for various studies on bulk polymers [19-24]. It will be shown in this section that the methodology is also capable of addressing polymer coatings.

This standardized scratch test has been employed in a number of recent studies to evaluate bulk polymer and coating performance [25-38]. There have also been investigations using finite element analysis (FEA) to correlate the stress states in coatings with adhesive strength, deformation and fracture behavior observed during scratch tests and nanoindentation experiments [39-49]. Since coatings are generally quite thin, often less than a few millimeters in thickness, the coupled effect between the substrate and the coating will introduce a great deal of complexity in the stress field that can only be addressed through FEA and material science studies.

It has been shown that the indenter tip geometry plays an important role in generating scratch damage [50]. Fortunately, the indenter tip geometry effect can be normalized by considering only the stress, not the load, applied to the coatings *via* FEA. To study the coating scratch behavior, it is important to establish a link between the observed coating damage to the material parameters, such as glass transition temperature (T_g), modulus, cross-link density, ductility, etc. [51-55]. The FEA modeling and material science studies will enable the construction of the structure-property relationship in the scratch behavior of polymeric coatings. It is intuitively clear that the thickness of the coating will also have an impact on the observed scratch behavior, and should be investigated.

This chapter will show the application of the recently standardized scratch test methodology mentioned above to characterize a set of experimental acrylic coatings with regards to ductility and coating thickness. It will be shown that this standardized method is effective in quantitative evaluation of the scratch resistance of coatings. The scratch damage mechanisms and their relation to material parameters will be discussed and remarks regarding the improvement of coating scratch resistance will be made.

Experimental

Model Material Systems

Model systems for this study consisted of a set of experimental acrylic coatings with their formulations listed in Table 1. The coatings were applied in different

thicknesses to phosphatized steel substrates prepared by Dow Chemical (Freeport, TX). The wet coatings were applied using a drawdown bar method and were then cured using ultraviolet light to obtain a uniform thickness. The coated steel coupons have dimensions of roughly 30 cm by 10 cm. The thickness of the uncoated steel plates is 0.813 mm. To measure the thicknesses of the coatings on the steel substrate, the thickness of the coated steel plate was first measured at several points and then averaged; the thickness of the uncoated plate was then subtracted from the above value to obtain the coating thickness.

TABLE 1**.** Formulations of model coating systems (parts per 100 weight).

Formulation	***A***	***B***	***C***
Dow Experimental Acrylate Oligomer[†]	-	24	35
Dow Experimental Acrylate Monomer[‡]	38	-	-
Bis A Epoxy Acrylate	57	47.5	30
Tri(propylene glycol) Diacrylate	-	24	25
Photo Initiators & Modifiers	5	4.5	10

[†] Average Functionality = 1.0; Avg. Mol. Wt. = 1060 (GPC); Viscosity @ 25oC = 470 cps
[‡] Average Functionality = 3.0; Calculated Mol. Wt. = 465; Viscosity @ 25oC = 140 cps

Mechanical properties of the model coatings systems (Table 2) were characterized at Dow Chemical. Tensile specimens were cut from cured acrylic films with a thickness of 0.152 mm. The cutter used was a Type IV tensile die cutter. The tensile stress-strain curves were generated according to ASTM D638 using a crosshead speed of 0.085 mm/s. The grip separation was 1 cm, which included the fillet section. Engineering strain was calculated from the crosshead displacement. Engineering stress was defined conventionally as the force divided by the initial unit cross-sectional area.

TABLE 2**.** Mechanical properties of model coating systems used for ductility effect study.

	Thickness (mil)	***Tensile Modulus*** (GPa)	***% Elongation at Break***	T_g (^oC)	***Rubbery Plateau Modulus*** (MPa)
A	2.1	2.6	1.2	102	45.1
B	1.6	1.3	4.6	71	49.8
C	2.2	0.49	6.8	54	41.4

Dynamic mechanical spectroscopy was obtained in tensile mode using a Rheometrics RSA-III instrument. A frequency of 1 Hz was used for testing and each test spanned a temperature range from 23 °C to 170 °C with a heating rate of 3 °C/min. The grip to grip distance was 15 mm and the sample width was 8 mm.

The effect of ductility will be addressed using the three coatings formulations given in Table 1. Coating C, which exhibited superior adhesion to the steel substrate, will be used to explore the coating thickness effect.

Scratch Testing

Even though ASTM D7207-05 outlines scratch test conditions, the parameters can be altered to accommodate the studied material. In this study, the scratch length was set at 150 mm, instead of the proposed 100 mm, to allow for more precise determination of the onset of critical loads for various scratch damage mechanisms. The test was performed using a linearly increased normal load from 1 N to 50 N at a speed of 100 mm/s and the tip used was a 1 mm diameter stainless steel ball. The load and displacement data were captured with LabVIEW and stored as a data file for later

analysis. Six tests were performed per sample and the values obtained were averaged for each coating system.

Quantitative Surface Damage Analysis

The scratch damage features were analyzed using images obtained with the flatbed PC scanner. The more detailed damage mechanisms of the experimental acrylic coatings were observed using a JEOL JSM-6400 SEM operated at an accelerating voltage of 15 kV. Two cm by 2 cm square sections of the coated steel substrates were cut around the points where the damage transitions were observed and were dried overnight in an oven at ~80 ^{o}F. To prevent charging of the coating surface, an AuPd coating of about 400 Å was applied with a Hummer sputter coater.

Results and Discussion

Ductility Effect

Figure 4 shows the engineering stress-strain curves for Coatings A-C and illustrates the variation in ductility for this part of the study. The key tensile properties of the three coatings are also listed in Table 2.

Scratched surfaces of the three Coatings were scanned using a commercial scanner and the representative images are shown in Figure 5. From these images, the effect of coating ductility can be readily observed.

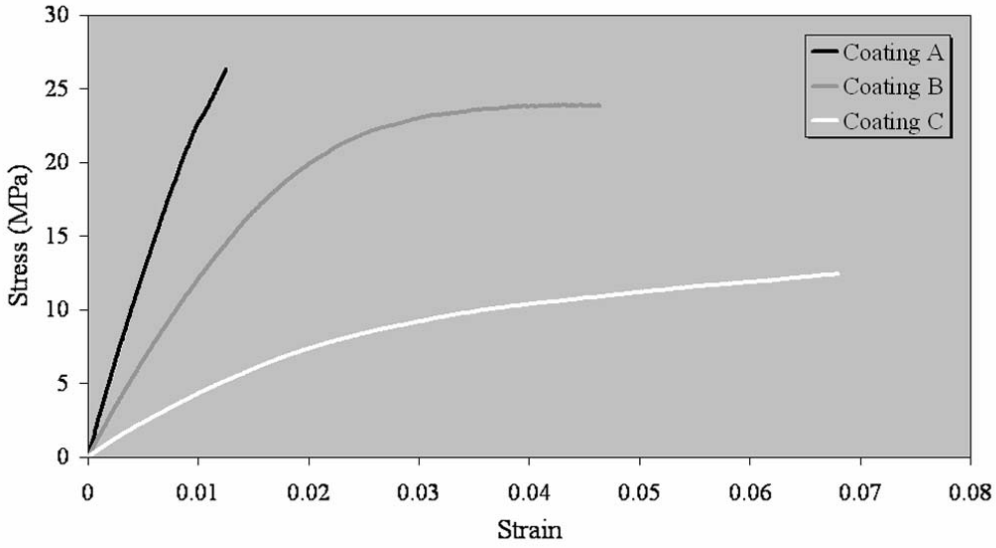

FIG 4. Engineering stress/strain curves for the experimental acrylic model coatings used to explore the ductility effect.

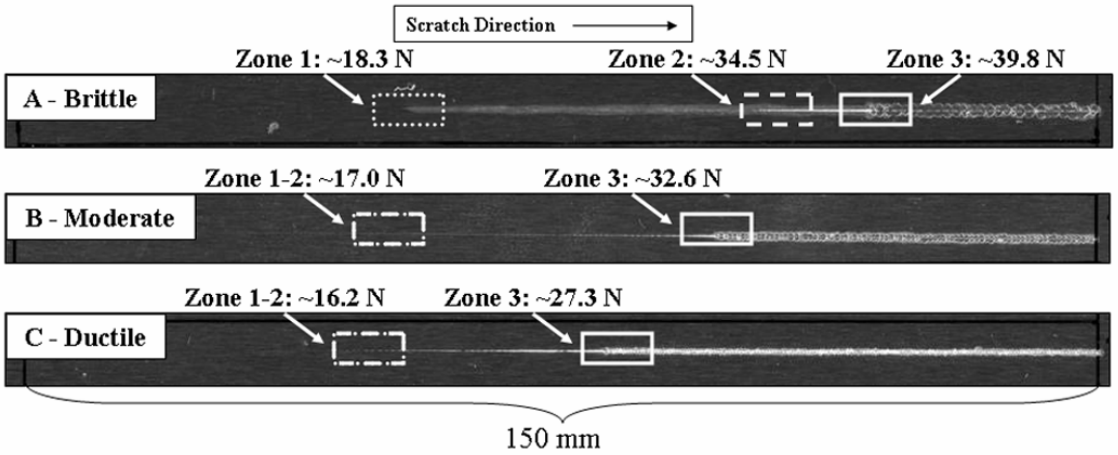

FIG 5. Images obtained from optically scanning scratched surfaces of Coatings A-C showing various damage regions of interest: Zone 1 = adhesive delamination, Zone 2 = microcracking, Zone 3 = coating failure (buckling) and exposure of substrate.

Zone 1 represents the transition from where the coating undergoes no damage to where the coating adhesively delaminates from the substrate, but otherwise remains cohesively intact. The adhesive delamination can be seen with the naked eye due to the reflection of light caused by the gap between the steel substrate and the delaminated acrylic coating. Using this principle, it can be seen that Coating A undergoes an extensive amount of delamination compared to that of Systems B & C.

However, Coatings B & C experience microcracking, observed in Zone 2, much sooner than that for Coating A. These microcracks were generated under the center of the indenter tip and radiate outward at 45° angles relative to each side of the scratch path (Figure 6a). At first, the cracks are locally isolated from one another until a critical load, and a resulting stress state, is reached where the cracks become interconnected, as shown in Figure 6b.

As the damage progresses with increasing normal load, eventually the indenter tip reaches the substrate and causes buckling to take place. This results in the removal of a small piece of material, consequently leaving the substrate exposed and even damaged by the indenter (Figure 6c). The buckling process is the cause of the damage seen in Zone 3.

The detailed damage features of Zone 3 for Coatings A-C shown in Figure 7 serve to illustrate the difference in mechanical properties and adhesion characteristics of the model coating systems. The region outlined by the dashed white lines indicates the region of coating that was delaminated, but otherwise remained intact. It is evident that Coating C exhibits the best adhesion to the steel substrate. It was for this reason Coating

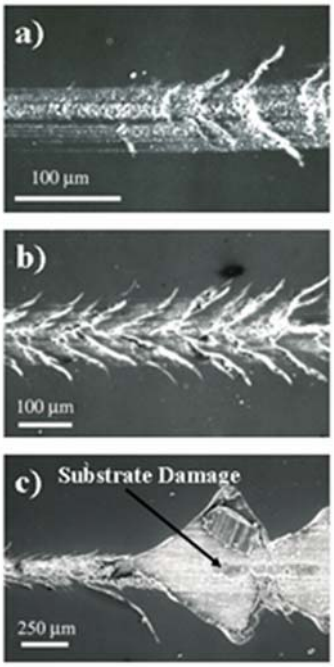

FIG 6. SEM micrographs showing a typical progression of cohesive damage associated with Zone 2: a) onset of microcracking (Zone 2), b) crack interconnection, c) transition from microcracking to onset of buckling (Zone 3). (Coating C shown as an illustrative example).

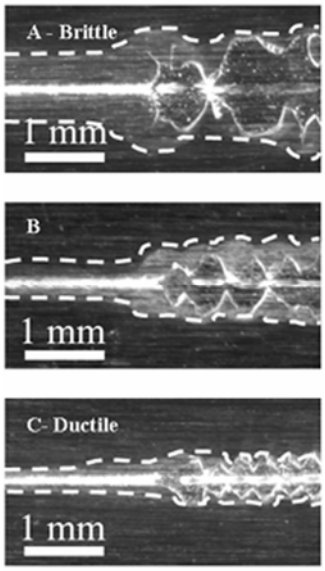

FIG 7. Closeup views of Zone 3 (from Figure 2) showing adhesive delamination (gray region outlined in white) associated with microcracking and buckling.

C was chosen as the model system to explore the effect of coating thickness on scratch behavior.

It is noted that, to fully evaluate the effect of ductility on scratch behavior, one should have coating systems that have the ductility as the only independent variable. Work is currently underway to obtain a set of model coating systems that have similar adhesive properties with varying ductility. Nevertheless, these results show the effectiveness of the standardized test methodology in quantitatively evaluating the scratch resistance of polymeric coatings.

Coating Thickness Effect

Several specimens of Coating C with thicknesses ranging from about 0.01 mm to just under 0.08 mm were utilized for this portion of the study. As many thicknesses of Coating C were actually analyzed using the methodology to observe any apparent data trends, three representative specimens with the thicknesses shown in Table 3 were chosen to illustrate the points of interest.

TABLE 3. Thicknesses of the representative specimens of Coating C used for the thickness study.

Coating	***Thickness***
C1	0.4 mil
C2	1.4 mil
C3	2.4 mil

Comparing the scanned images for Coatings C1-C3, a trend showing a diminishing thickness dependency becomes clear (Figure 8). The onset points,

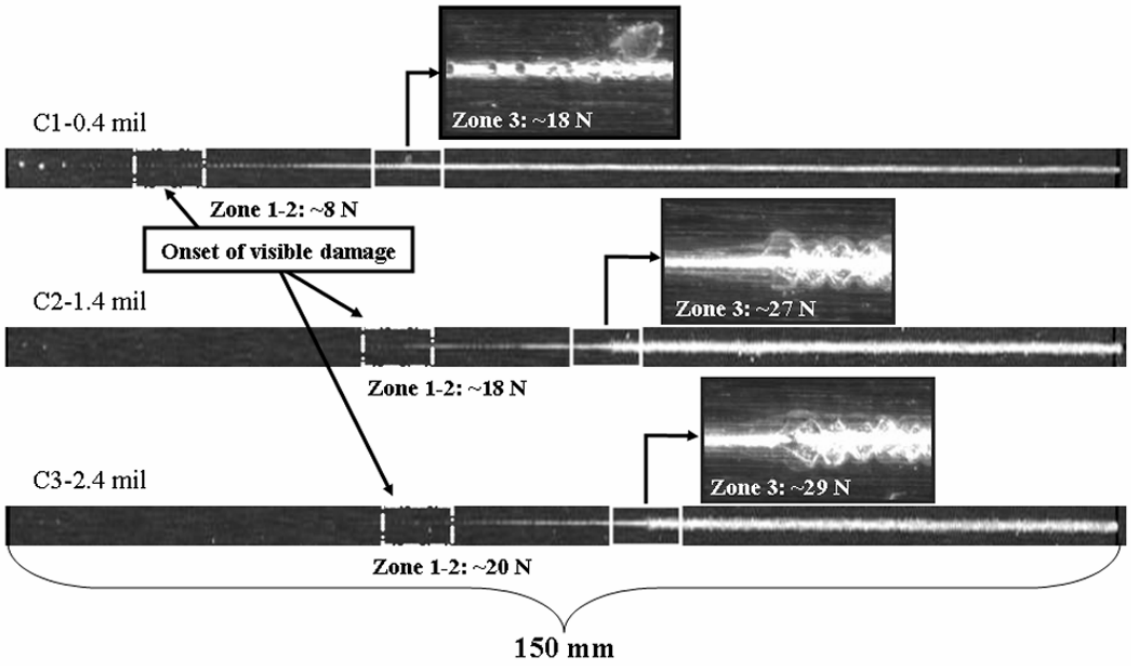

FIG 8. Images obtained from optically scanning scratched surfaces of Coatings C1-C3 showing various damage regions of interest: Zone 1 = adhesive delamination, Zone 2 = microcracking, Zone 3 = coating failure (buckling) and exposure of substrate.

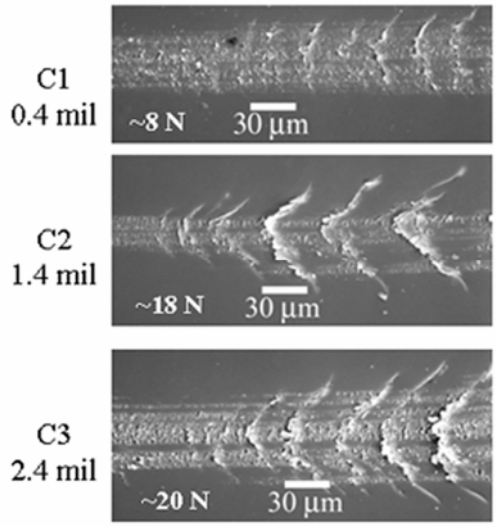

FIG 9. SEM micrographs of the onset of transverse cracking (Zone 2) for Coatings C1-C3.

regardless of the damage mechanisms, occur much sooner for C1 than for C2 and C3. There is not a great difference between C2 and C3. SEM micrographs verify this trend when viewing the microscale features of Zones 2 and 3 (Figures 9 and 10, respectively). Compared to C2 and C3, the transverse cracks in Figure 9 are not as severe at onset for C1 and the buckling feature mechanism in Figure 10 appears to be more gradual. Again, no discernible difference can be seen in C2 and C3 regarding the appearance of these microscale features.

From Figures 5 and 8, it should be noted that the maximum width of the coating fracture zone remains fairly constant. This is believed to be because, after the indenter begins to touch the substrate under a high normal load, the same amount of material is removed each time the coating experiences buckling failure. Figure 11 illustrates how the maximum width of the fracture zone is defined. Due to the fact that this feature apparently exhibits a similar trend as for the other features of interest, it can be used as a parameter to provide further insight to the effects of coating thickness.

Figures 12 and 13 summarize the values for the properties of interest obtained for Coating C over the range of available thicknesses. The effectiveness of this methodology is plainly indicated by the small standard of deviation, as shown in Figure 12. The apparent trend observed thus far becomes evident in Figures 12 and 13. There appears to be an increase in each property as thickness increases to about 0.036 mm, after which the values seem to experience a plateau effect. This implies that there is a critical coating thickness at which the material will be able to withstand the most scratch

damage under scratch loading. The exact mechanical reason for such a leveling off phenomenon will be addressed *via* FEA in future studies.

Research is currently underway using FEA to correlate the stresses at the interface between the coating and the substrate with the delamination and scratch damage observed. Successful research leading to fundamental knowledge of structure-property relationships in coating scratch behavior will pave the way for the analytical design of scratch resistant polymeric coatings.

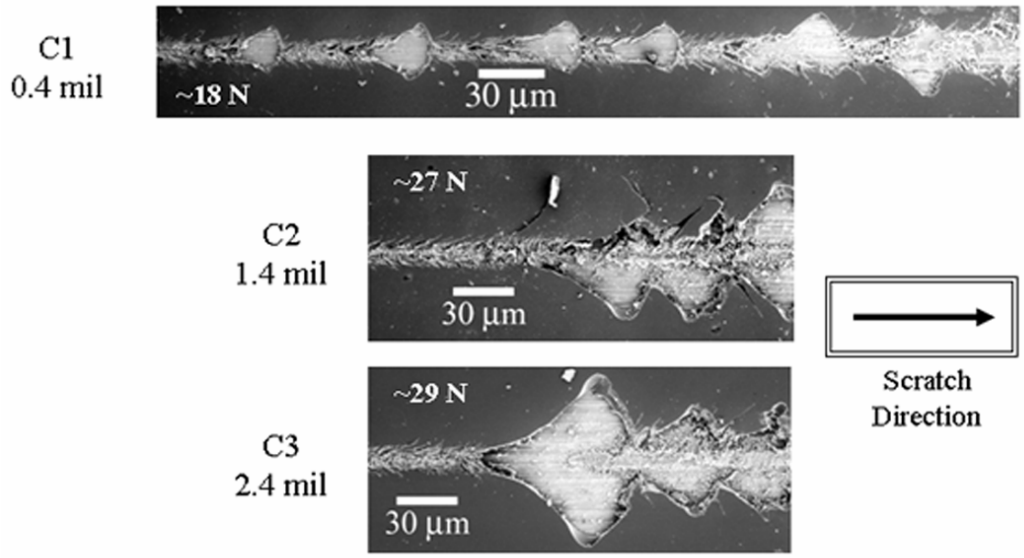

FIG 10. SEM micrographs of the onset of buckling (Zone 3) for Coatings C1-C3.

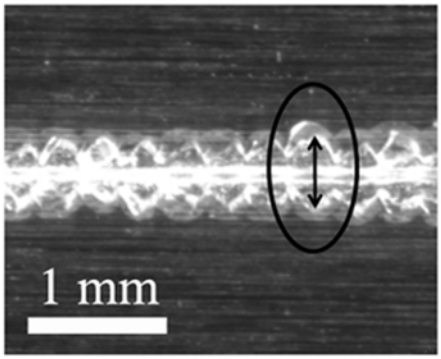

FIG 11. Close-up of the damaged region of Coating C after the onset of buckling (Zone 3) showing a consistent maximum width of the fracture zone.

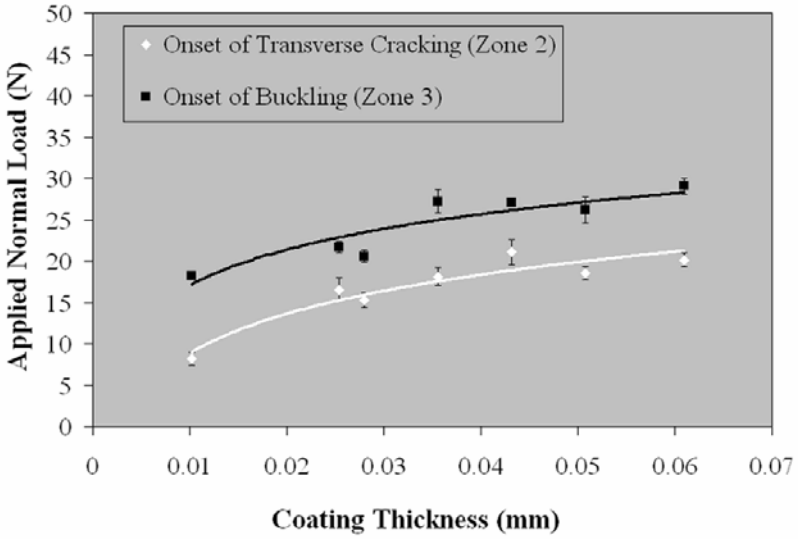

FIG 12. Critical load for the onset of transverse cracking in Zone 2 and the onset of buckling (Zone 3) as a function of coating thickness.

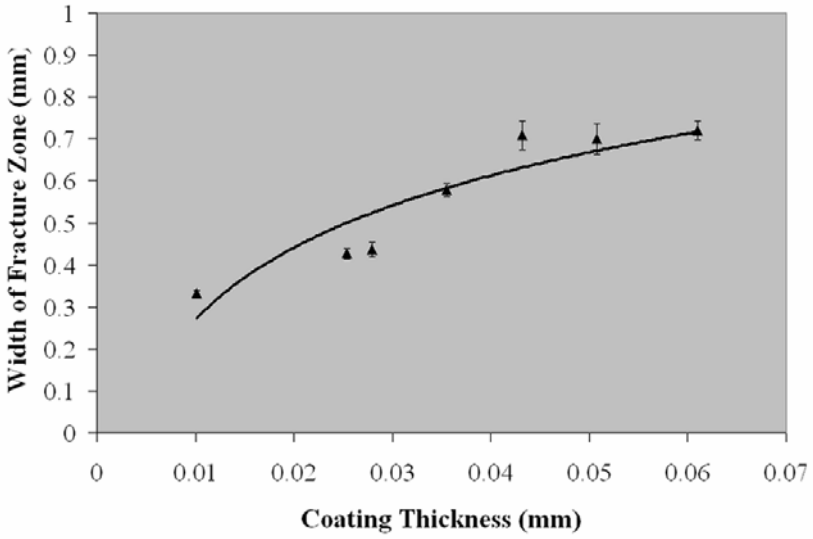

FIG 13. Width of fracture zone in Zone 3 as a function of coating thickness.

CHAPTER III

EFFECTS OF SLIP AGENT AND TALC SURFACE TREATMENT ON THE SCRATCH BEHAVIOR OF THERMOPLASTIC OLEFINS

As stated previously, material property tradeoffs must often be compensated for. For polypropylene (PP) applications, it is desired that parts manufactured from this material will be able to operate in most climates. Polypropylene becomes extremely brittle and exhibits poor impact strength at low temperatures. For applications such as exterior automobile panels, this becomes a problem in winter climates where the temperature can register below 0 degrees Fahrenheit.

As a solution, the PP is subjected to a reaction with propylene and ethylene. The ethylene and propylene form a rubber phase within the PP matrix known as ethylene-propylene rubber, or EPR. This rubber-modified PP blend, known as a thermoplastic olefin (TPO), has gained wide acceptance for application in the automotive industry due to its light weight, superior impact performance, ease of recyclability and low cost [19, 56]. The main benefit, however, is that the incorporation of the EPR significantly reduces the glass transition temperature (T_g) of the TPO to a point where it can be used in the cold climates where PP cannot.

It has been shown that TPOs exhibit relatively poor scratch resistance as compared to other engineering polymers [23]. Despite that, the use of TPOs continues to be attractive to the automotive industry due to their low material and manufacturing cost.

A way of improving the scratch resistance of TPOs is by modifying the constituents of the material system *via* the introduction of fillers (e.g., talc) and specialty additives (e.g., slip agents). It has been shown by recent studies [22, 24, 57, 58] that incorporating talc in TPOs can help to increase their stiffness and scratch hardness [22], in addition to lowering the manufacturing cost of finished products. Known to have poor bonding properties with polymer matrices, pristine talc can easily be debonded due to surface deformation and damage [57]. For the inherent white color of talc, scratch visibility can be increased due to light reflection from exposed talc particles. With special surface treatment of talc filler, not only can the bonding with polymeric materials be improved, and improvement in talc dispersion throughout the matrix can also be achieved.

Slip agents, like oleamide and erucamide (chemical structures shown in Figure 14), are long-chain amides, and are derived from fatty acids. During the blending process with a polymeric matrix, the unique thermo-chemical properties of oleamide and erucamide allow these molecules to migrate to the surface as the polymer melt cools in a process known as "blooming" [59]. After the erucamide has migrated to the TPO surface, it forms a thin, waxy layer that lowers the coefficient of adhesive friction and also aids in mold release. Slip agents are also being used in the processing of linear low density polyethylene (LLDPE) films where the surface lubrication allows the film to slide over itself for better product handling and easy storage [60-63]. For its stability at high processing temperatures, erucamide is generally preferred over oleamide for polypropylene applications [64].

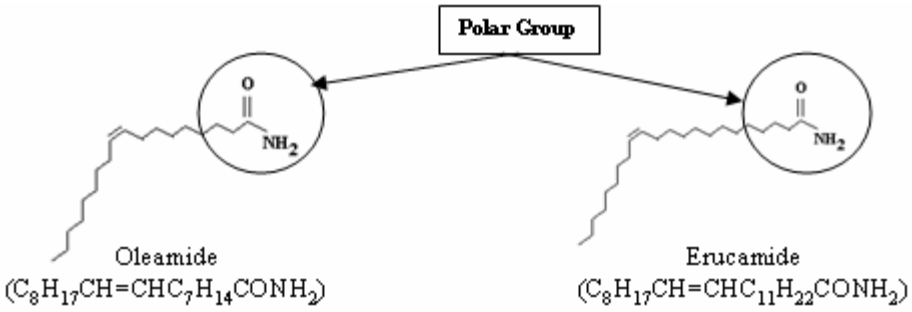

FIG 14. Chemical structures of commonly used slip agent additives.

The objective of this portion of the work is to examine the effect of the addition of surface-treated and untreated talc as well as erucamide on the scratch performance of TPOs. Four TPO systems incorporating different types of talc and varying concentration of erucamide will be considered. Using the established evaluation and testing methodology and using various established materials science tools including scanning electron microscopy (SEM) in both backscattering and secondary modes, optical microscopy (OM) and Fourier transform infrared spectroscopy (FTIR), the scratch damage mechanisms of these material systems will be carefully examined. Approaches for improving scratch resistance of TPOs will also be presented.

Experimental

Model Material Systems

Four material systems (Systems A-D) were used in this study with the constituents and their weight compositions found in Table 4. Talc fillers ($Mg_3Si_4O_{10}(OH)_2$) were provided by Luzenac North America in both surface-treated

(R7) and untreated forms (Cimpact 710) and the constituents were injection molded into plaques (16 cm by 8 cm by 0.3 cm). Carbon black was used as a colorant to provide adequate visible contrast for the scratch visibility investigation. For comparative purposes, Systems A-C were used to explore the effect of the slip agent while the effect of talc surface treatment was investigated using Systems B and D since they have the same amount of slip agent (0.3 wt%) but different types of talc filler.

TABLE 4. Weight compositions of the model systems investigated.

System	*PP/EPR Copolymer*	*Untreated Talc*	*Surface Treated Talc*	*Slip Agent*	*Color*
A	78 %	20 %	-	-	~3 %
B	78 %	20 %	-	0.3 %	~3 %
C	78 %	20 %	-	0.6 %	~3 %
D	78 %	-	20 %	0.3 %	~3 %

Scratch Testing

Specimens of the four material systems were tested at room temperature using the Scratcher III according to the standard conditions stated explcitly in ASTM D7207-05 [1]. The tip used was a stainless steel ball bearing with a diameter of 1-mm. Real-time normal and tangential load data were captured and later correlated to the scratch damage that occurred during testing.

Scratch Visibility Evaluation

The scratched surfaces of Systems A-D were subjected to the scratch visibility criteria previously discussed.

Scanning Electron Microscopy

SEM was conducted in both backscattering and secondary modes using a JEOL JSM6400. For backscattering imaging, unscratched samples of Systems A-D were cut into small blocks (3-mm by 6-mm) and the cross-section edge (perpendicular to the scratch path) was cut smooth using an Ultracut microtome equipped with a cryogenic diamond knife (Microstar) at room temperature. A Cressington 308 coater, operated at a vacuum of 0.01 Pa (10^{-6} mbar) and 8 volts, was employed to deposit a thin layer of carbon (~15 nm) on the sample surfaces to prevent charging.

Larger blocks (1-cm by 3-cm) of scratched samples of the four systems were utilized for the secondary mode observation. These blocks were dried overnight in an oven at 80°F and then coated with AuPd (~400 Å) using a Hummer sputter coater to prevent charging. An accelerating voltage of 15 kV was used for both modes of imaging.

Fourier Transform Infrared Spectroscopy

For FTIR evaluation, a Nicolet Avatar 360 was employed in attenuated total reflectance (ATR) mode to determine chemical spectra of virgin surfaces of Systems A-D and powdered erucamide. Spectra were taken for five specimens of each system and then averaged to yield a representative spectrum of the material.

Optical Microscopy

Sections of scratched surfaces were cut (~1-cm by 2-cm) and cast into epoxy blocks. Using a disc polisher, specimen surfaces of Systems A and D were polished to view scratch damage using an Olympus BX-60 optical microscope in reflectance mode.

Results and Discussion

Various material science and scratch evaluation methods including image analysis, SEM, OM and FTIR were employed to interpret the findings of this study.

Scratch Visibility Evaluation

Figure 15 displays scanned images of the scratched samples of Systems A-D that were processed with the gray-scale threshold option in ImageJ (Threshold: 40-255). Using this option, a clear difference in the scratch resistance of these systems can be obtained in an objective manner. The critical load for the onset of scratch visibility of was calculated using Equation 1 and is shown for each system in Figure 15. It can be clearly seen from these results that System D shows the highest resistance to scratch visibility. The trend in scratch visibility seen in Figure 15 corresponds to the averaged critical loads presented in Figure 16.

However, it is counter-intuitive that System D shows the best resistance to scratch visibility, due to the fact that it has only half of the concentration of slip agent as that of System C. This anomaly in the scratch performance will be addressed later. It

FIG 15. Processed images of Systems A-D showing onsets of visible damage obtained using the grayscale threshold option in ImageJ and corresponding critical loads.

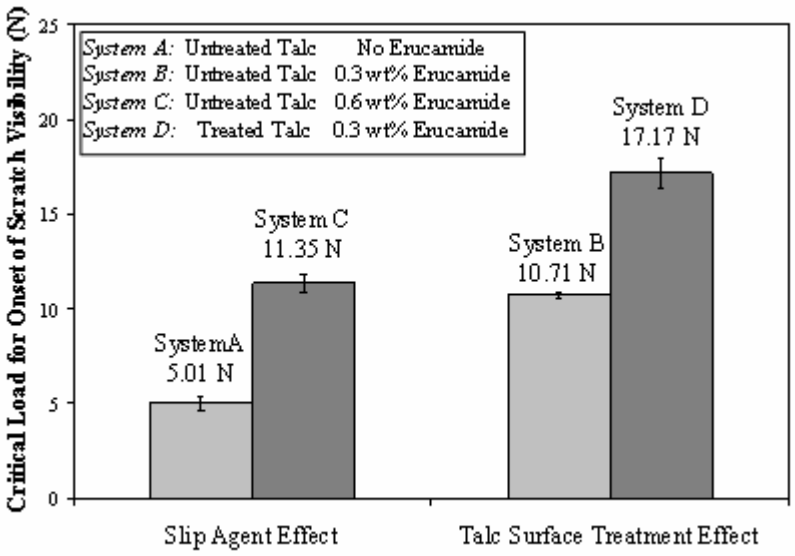

FIG 16. Critical load for onset of scratch visibility, F_c, for Systems A–D.

should be noted that doubling the concentration of erucamide in the untreated talc systems does result in an appreciable improvement in scratch visibility. Furthermore, by comparing both Systems B and D, it implies that the surface treatment of talc has a positive effect in improving the scratch resistance of TPOs.

Frictional Behavior

The scratching coefficient of friction (SCOF) curves for Systems A-D are presented in Figure 17. The curves represent the average values obtained from five specimens of each system. The region labeled as "Zone 1" in Figure 17 is the portion of the scratch where a noticeable difference can be discerned in System D relative to the other three systems; while in Zone 2, the SCOF of Systems A-D begin to converge towards the end of the scratch path. Figure 17(b) shows that among all, System D has the lowest SCOF in Zone 1, but converges with Systems A-C in Zone 2. Noting that erucamide, when migrated to the polymer surface, can help to lower the coefficient of adhesion friction, it is suggested that Zone 1 represents the portion of a scratch where erucamide has the most influence on the scratch behavior. Additionally, the trend in the results for SCOF correlates well with those for visibility and critical load and hence supports the claim on the improvement in scratch visibility.

Scratch Hardness

As discussed, scratch widths were measured at several points from the scanned images and the corresponding normal loads were calculated for each point using

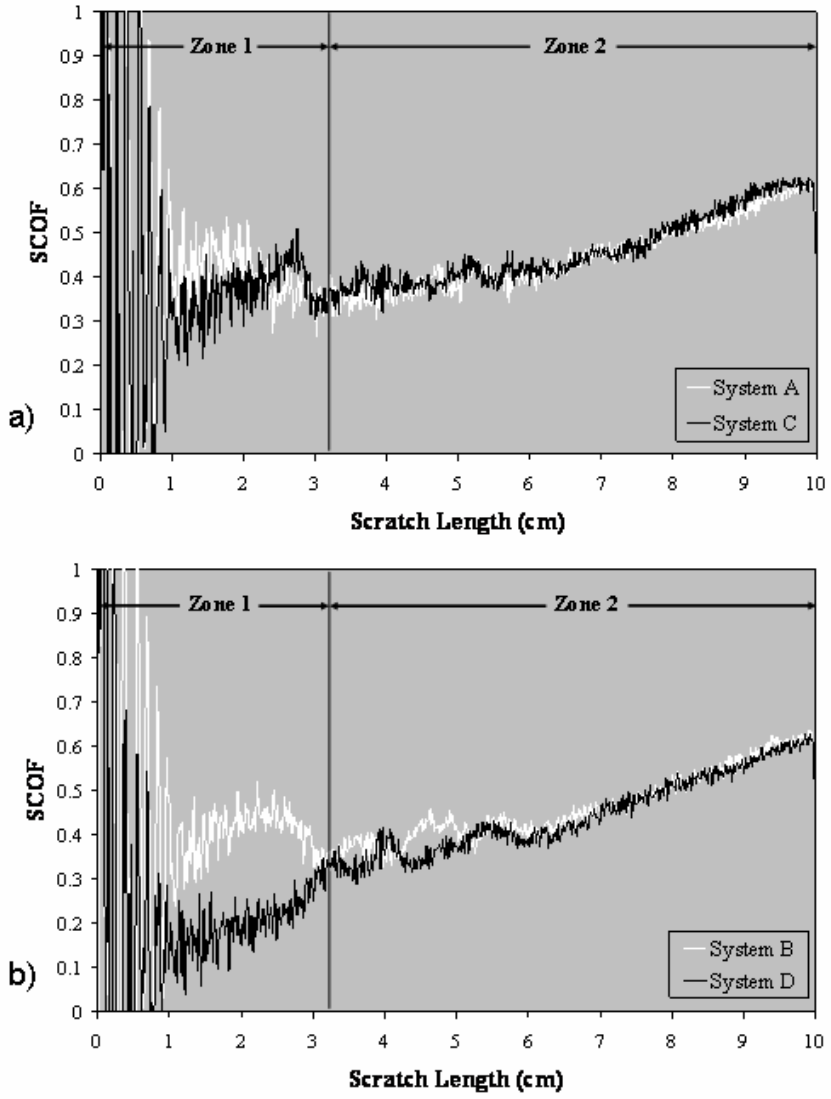

FIG 17. Scratch coefficient of friction (SCOF) for a) systems A & C and b) Systems B and D.

Equation 1. The linear regression fit of the plot of applied normal load against contact area (calculated with Equation 2) showed reasonably linear behavior. Thus, the average of five samples for each system was taken as the scratch hardness of that specimen.

The results in Figure 18 show that there is no appreciable difference in the scratch hardness of the four systems. This suggests that scratch hardness, which depends on the overall size of scratch damage, is not affected by the TPO modifications in this study. This also means that the amount of erucamide migrated to the TPO surface may not be significant to change the overall damage size. Most importantly, the measurement of scratch hardness does not take into account of the possible variations in polymer damage mechanisms, *i.e.*, ductile (yielding) or brittle (crazing/cracking). As a result, the scratch hardness values cannot be correlated to scratch visibility. Nevertheless, scratch hardness can still be a useful parameter to quantify scratch performance provided that the scratch mechanisms observed in the systems of interest are the same.

Aggregation of Talc Filler

To explore the unusual trend that System D, which has only half of the concentration of erucamide of System C but with surface-treated talc, has the best observed scratch performance, investigation was performed on cross-sections of Systems A-D using the backscattering mode of SEM to provide elemental contrast of the materials in the matrix. Figure 19 displays images obtained from the backscatter imaging effort and shows that Systems B and C contain large aggregate of talc particles.

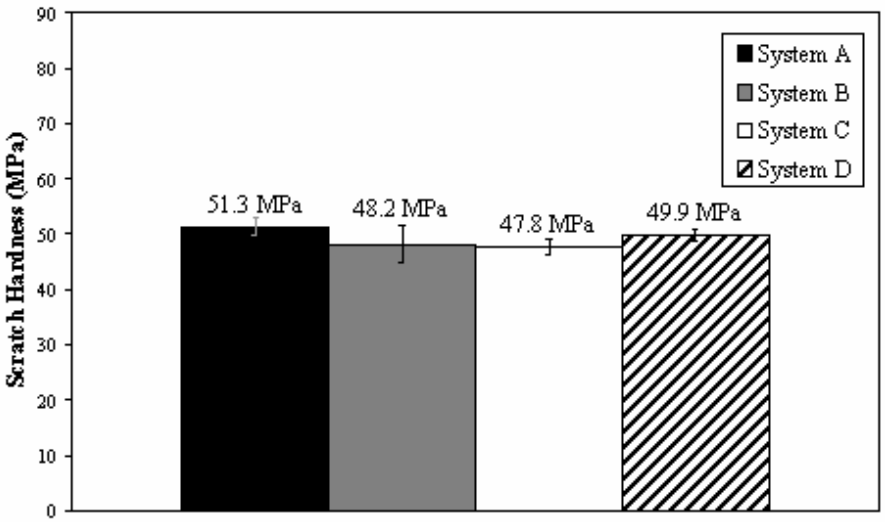

FIG 18. Scratch hardness for Systems A-D.

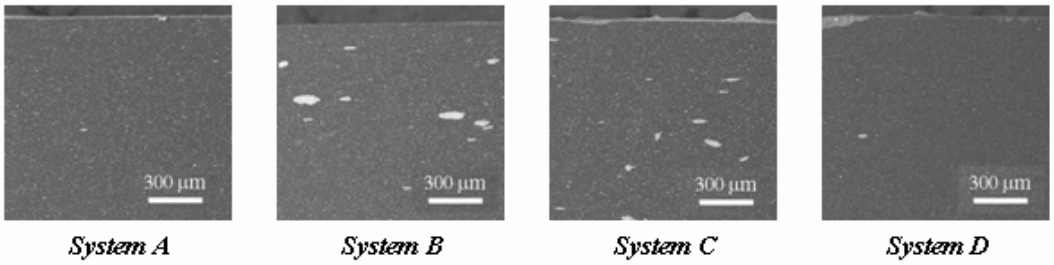

FIG 19. Backscattered images of cross-sections of Systems A-D displaying aggregate particles. (White spots indicate talc aggregation).

These aggregate particles can form stress-concentration points within the matrix that can lead to premature failure and stress-whitening. By comparing System A to Systems B and C, one can also infer that the presence of erucamide may play a role in promoting the aggregation of untreated talc.

To further explore the effect of talc surface treatment, an additional material system, which contains only surface-treated talc and no slip agent, was also tested and subjected to the same SEM observation. No sign of aggregation was observed (not shown). This implies that without the slip agent, surface treatment of the talc alone is insufficient to induce aggregation. The absence of aggregations in System D suggests that good global dispersion of surface-treated talc fillers is achieved and leads to the speculation that there is a physical interaction between the untreated talc and erucamide to cause the formation of the aggregate particles as seen in Systems B and C.

It is believed that erucamide is being adsorbed onto the surface of the untreated talc filler. It is well known that the surface of talc is hydrophobic in nature, but the polar hydroxyl groups present on the talc edges could possibly possess an affinity for the polar amide end group in the erucamide. Once erucamide is adsorbed onto the talc particles, lesser amount of erucamide will be migrated to the polymer surface for lubrication.

It should be noted that, despite an exhaustive effort by using various microscopy and spectroscopy tools to locate erucamide on the aggregated talc particles, no direct evidence of erucamide on the aggregated talc particles can be found owing to the low concentration of erucamide and the small size of the aggregate.

Spectroscopic Analysis

Figure 20 is a transmission FTIR spectrum of a neat sample of erucamide with the intense peak at 1645 cm^{-1}, which will be used to characterize its presence on the surface of Systems A-D, much in the same manner as in the work of Joshi and Hirt for LLDPE films [60]. Figure 21 presents the FTIR-ATR spectra taken on virgin surfaces of Systems A-D. The peak at ~1460 cm^{-1} is unique to the PP/EPR matrix [65].

To verify that the resulting FTIR peaks in System D did indeed correspond to erucamide, the spectrum for System A was subtracted from System D. The resulting spectrum showed the same peaks shown in Figure 20 with the most intensity being at 3400 cm^{-1} and 1645 cm^{-1} due to the N-H stretch and the C=O stretch in the amide end group of erucamide, respectively. The spectrum range displayed in Figure 21 because this range provides the most evidence of the presence of erucamide on the TPO surface due to the high intensity contrast in the peaks representing the erucamide and the PP/EPR matrix.

From Figure 21, System D shows the highest relative peak intensity for erucamide. This indicates that System D has the highest surface concentration of erucamide. From these spectra, it is clear that certain amounts of erucamide in Systems B and C did not migrate successfully to the surface. As discussed above, it is likely that the erucamide is being trapped within the matrix and possibly adsorbed onto the untreated talc filler surface.

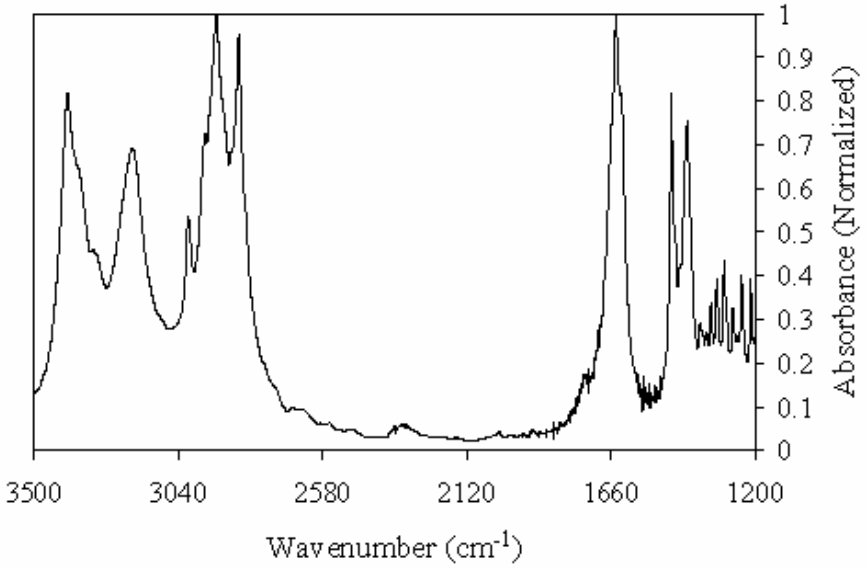

FIG 20. FTIR spectrum of neat erucamide.

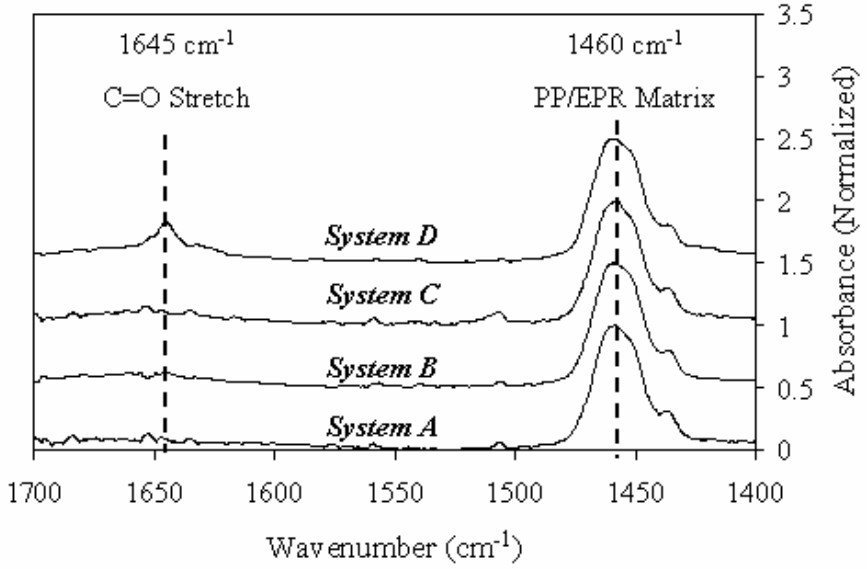

FIG 21. FTIR-ATR spectra of virgin surfaces of Systems A-D.

Surface Scratch Damage

SEM imaging with secondary electron scattering mode was also performed to observe how talc fillers affect the scratch damage features on the surface of the four model TPO systems. For all four systems, two damage transitions can be noted, as shown in Figure 22. The first transition is where the scratch evolves from a smooth and depression-like feature to a rough and "fish-scale" pattern where the material under the tip is pulled along the scratch direction in a ductile manner. This rough pattern scatters light more than the smooth feature and causes the damage to become more visible. From the earlier discussion on scratch visibility, the values of F_c are based on the onset of visible damage caused by light scattering. A detailed examination reveals that the point at the onset of the fish-scale feature occurs slightly earlier than the critical point found for F_c. This is because the scratch damage feature starts out small and scarce and then progresses in size and regularity. As a result, the point where the surface damage can be detected by the visible eye will not occur until the damage is severe enough to scatter a sufficient intensity of light. A second transition occurs as a result of the material being fractured and torn away when the normal load increases to a point where the stress state exceeds the ultimate strength of the material.

For System D, the two transitions occur at much higher normal loads than Systems A-C and a significant difference can be noted in the damage features at the second transition. Owing to this fact, the surface-treatment of the talc filler appears to enhance the TPO/talc interaction which will ultimately allow for enhanced resistance to surface damage resulting from better erucamide migration. In addition, the damage at

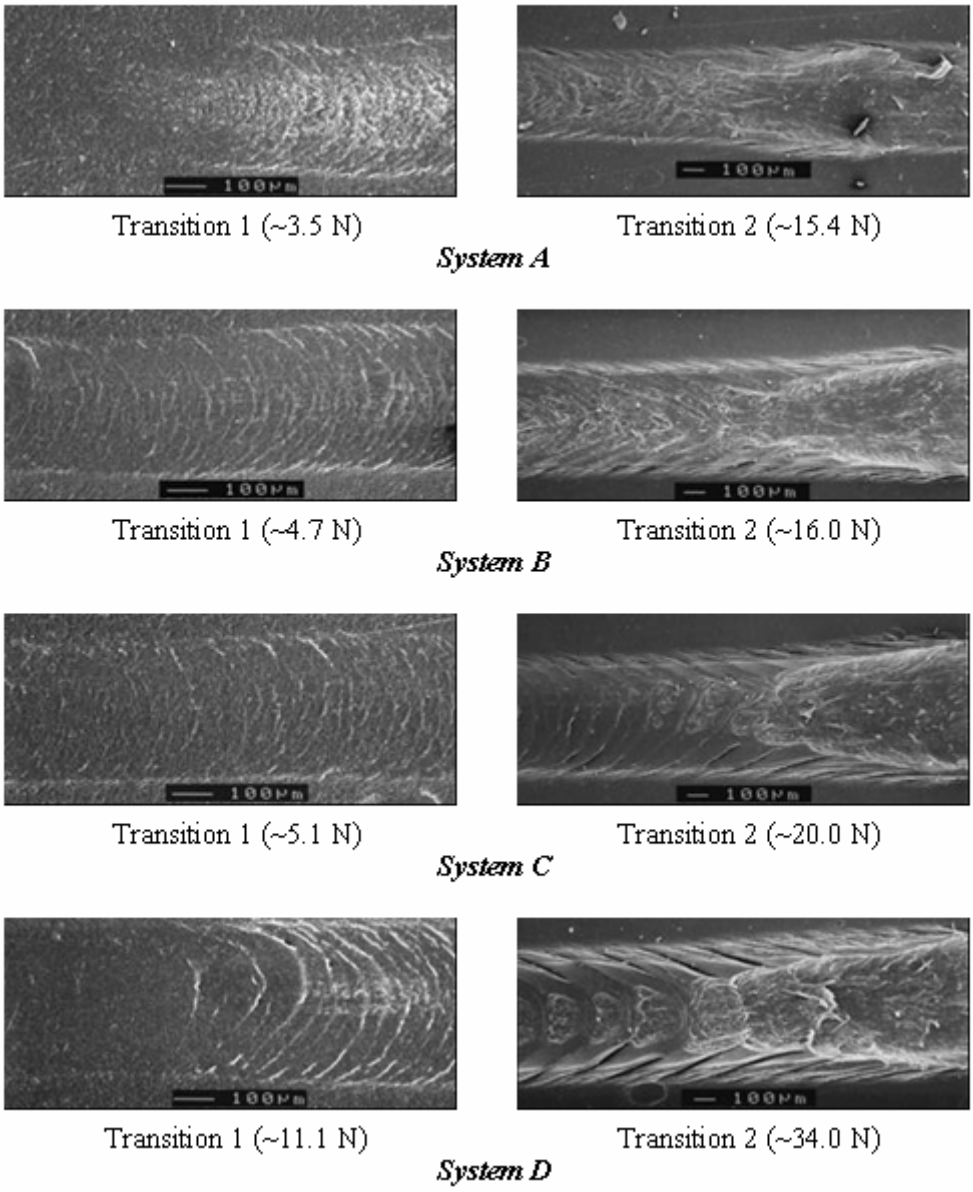

FIG 22. SEM micrographs of scratched surfaces of Systems A-D.

the second transition of System D possesses more regularity than other systems, which can be attributed to the additional amount of erucamide on the surface to provide more surface lubrication, as earlier shown in Figure 21. The extra lubrication allows the tip to slide easily over the surface, delaying the point where material drawing occurs. As a result for System D, the ductile drawing of the materials occurs over a longer period of time before the ultimate strength of the material is reached and is finally torn away.

It is noted that, for the surface-treated talc system that contains no erucamide (not shown), the first and second transitions occur at comparable normal loads to System A. This suggests that surface treatment of talc fillers by itself does not alter the surface damage features.

Subsurface Scratch Damage

The subsurface scratch damage was characterized using an Olympus BX-60 optical microscope in reflectance mode to measure the scratch depth with respect to the far-field flat surface. Cross-sections of Systems A and D at three points along the 100-mm scratch length (20-, 50- and 80-mm marks) are shown in Figure 23. The measurements of scratch depths of these three points yield lower values for System D. This could be a result of the improvement in the mechanical stiffness of the system from the better bonding of surface-treated talc to the polymer matrix or the presence of erucamide on the surface, or both. Note that scratch widths can also be obtained from the images shown in Figure 23 using the definition of scratch width in [21].

The present study points to the fact that an apparent interaction between untreated talc and erucamide in TPO can be avoided through surface-treatment of the talc filler. As a result, better migration of the erucamide to the TPO surface is achieved. The high level of surface lubrication gained from the high surface concentration of erucamide results in an optimal scratch performance over systems containing untreated talc. This indicates that care should be taken if multiple additives are to be incorporated in TPOs, especially when slip agent is to migrate to the TPO surface, to improve scratch resistance.

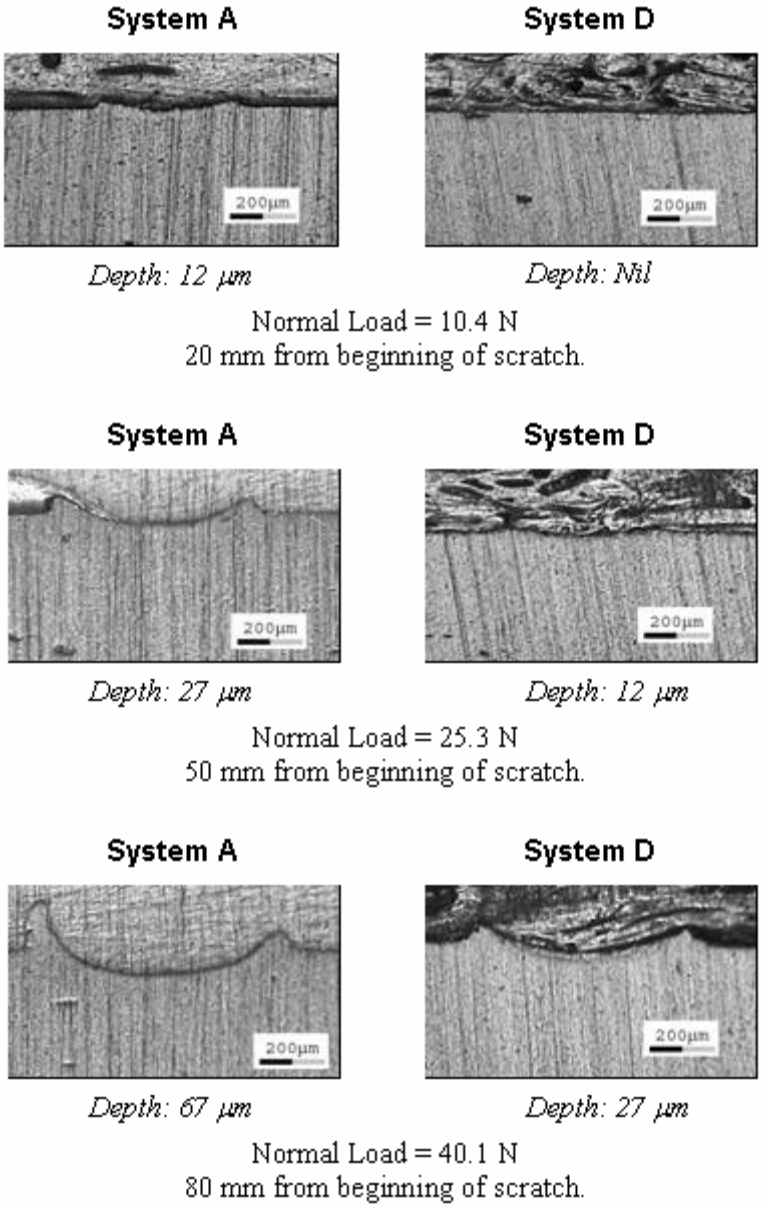

FIG 23. Optical micrographs of post-scratch cross-sections of Systems A and D.

CHAPTER IV

CHARACTERIZATION OF SURFACE ANISOTROPY AND ITS EFFECTS ON THE SCRATCH BEHAVIOR OF INJECTION-MOLDED POLYPROPYLENE

Mentioned in the previous chapter, injection molding is an efficient means to achieve rapid production of high-quality functional polymer parts. The main attraction of this method is the short cycle time that is required to make a molded polymer. In order to accomplish this, the polymer must be injected in molten form under high pressure into a mold where the temperature of the walls must be significantly lower than that of the melt. In addition, the thickness of the finished part must be adequately thin to facilitate fast cooling of the polymer inside of the melt.

Rapid cooling of semi-crystalline polymer melts under flow conditions introduces molecular orientation. As the melt flows, the molecular chains are oriented in the flow direction. However, upon contacting a cooler surface, the chains become, in effect, "frozen" in their flow state, thus preserving the orientation. In injection molding, the polymer melt is surrounded by cold mold walls. This introduces molecular orientation in the outermost layer of the polymer melt, resulting in an oriented, amorphous skin layer. The remainder of the polymer will continue to cool non-uniformly allowing for more relaxation of the polymer chains. The resulting morphology has been given the term "skin/core" and has been studied extensively [66-70].

In light of the fact that the cooling rate decreases as the distance from the wall to the center of the mold increases, it follows that the crystallinity of the cooled polymer will increase with increasing distance from the mold wall. This has been shown numerous times by showing the differences in birefringence of the different layers under cross-polarized optical microscopy [66, 71, 72]. The term "skin/core" can be misleading and is used to be concise when describing the final morphology. Since the cooling rate decreases gradually away from the mold wall, the crystallinity will also increase gradually. This will ultimately result in the creation of a transition layer, or layers, between the skin and the core. These transition layers are subject to high shear stress since it is between a layer of minimum velocity (skin) and a layer of maximum velocity (core). The existence of these layers can be easily shown through their differing birefringence, but characterizing their mechanical properties can prove difficult due to their thickness.

Fortunately, there have been numerous intents on exploring the molecular orientation of these different layers using infrared dichroism. Samuels showed the usefulness of this technique in characterizing the molecular orientation in isotactic PP films. His work showed the comparison of applying the Herman's orientation function, normally used for wide angle X-ray diffraction, to infrared dichroism using the dichroic ratio, D [73]. Samuels also measured the angle between the transition moment of the infrared vibration and the chain axis for several frequencies of the PP spectrum that relate to different phases of the material [74]. The principles of this work were then used by Strebel, et al. to quantify the degree of molecular orientation in the cross-sections of

injection-molded PP and TPO materials after tensile testing [75]. Their work shows that there are significant differences in the degree of orientation of the morphological layers of injection-molded polymers and that a high level of orientation exists in the skin layer.

This raises issues where scratch damage is of concern. Depending on the direction and extent of molecular orientation in the skin layer, the propensity for material displacement and deformation could change. As a result, the surface damage incurred by the polymer could vary with orientation of the scratch direction. However modification of the surface by the addition of a slip agent like erucamide might aide in alleviating anisotropic effects.

One can safely assume that the standardized scratch test can and will provide meaningful information regarding the mechanical behavior of the skin layer, as this layer will be most vulnerable to scratch damage. This chapter will show the effects of scratch direction relative to melt flow on the scratch behavior of injection-molded PP using the ASTM scratch test methodology as well as present the results of efforts to characterize the anisotropy induced by the injection molding process through infrared dichroism measurements and nanoindentation experiments.

Experimental

Model Material Systems

The samples tested in this study were injection-molded isotactic polypropylene plaques of dimensions 160 mm by 80 mm by 3 mm. One set of plaques

contained 0.5% by weight of erucamide and all plaques contained 2% by weight of carbon black for visibility contrast. The plaques were injection molded with the mold walls at ambient temperature (~75 ^{o}F) and a hold time of 13 seconds. The MFR of the i-PP was 35.

Scratch Testing

To accommodate for the geometry of the PP plaques, the scratch length for these specimens was set at 60 mm. The samples were tested under a 1-40 N linearly increasing normal load at a velocity of 60 mm/s using the 1 mm spherical scratch tip. As in the other studies, the real-time load and displacement data was recorded for post-mortem analysis.

Scratch Visibility Evaluation

The samples were analyzed using the previously discussed image processing techniques discussed earlier.

Scanning Electron Microscopy

Sections of the tested systems were cut and viewed in secondary mode using a JEOL JSM6400 SEM operated at an accelerating voltage of 15 kV. The specimens were dried overnight in an oven at 80°F and then coated with Au-Pd (~400 Å) using a Hummer sputter coater to prevent charging.

Fourier Transform Infrared Spectroscopy

Skin layer orientation was evaluated using IR dichroism on unscratched surfaces of the neat PP samples in attenuated total reflectance (ATR) mode by engaging a ZnSe polarizer directly in the laser path of a Nicolet Avatar 360. Each spectrum consisted of 32 scans in the center of the plaque at a resolution of 2 cm^{-1}. Two spectra were obtained. The second spectrum represents a 90^{o} rotation of the specimen relative to the previous sample orientation.

To detect the evidence of erucamide on the surface of the PP, FTIR was conducted in the same manner as for the TPO materials in the previous chapter.

Nanoindentation

To establish any difference between the nanomechanical properties of the morphological features beneath the skin relative to the melt flow direction, hardness and reduced modulus values were obtained using a Hysitron Triboindenter equipped with a Berkovich diamond tip. The applied load function is given in Figure 24. Indentations were made using a vertical spacing of 10 μm and a horizontal spacing of 30 μm for a vertical depth of 300 μm in an attempt to quantify the anisotropy through the depth of the skin region. The nanoindentations were made in the cross-section face of the neat bulk polypropylene so that the MFD was in the same direction as the Z-axis for one set (along melt flow) and the MFD perpendicular to the Z-axis for the other set (transverse to melt flow) (Figure 25). Triboscan 6.0 (Hysitron, Inc.) software was used for test execution and data analysis.

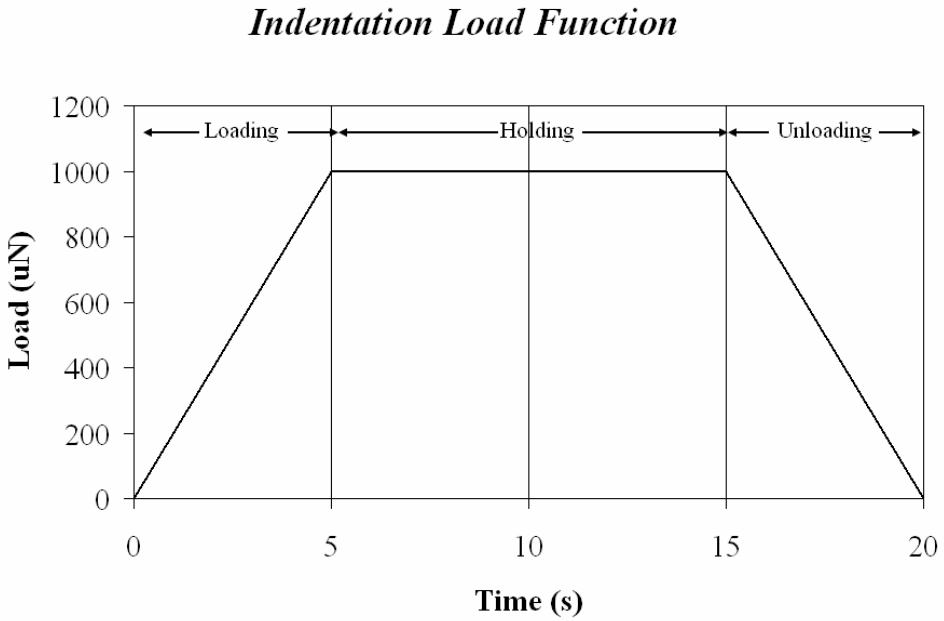

FIG 24. Load function used for nanoindentation of injection-molded PP samples.

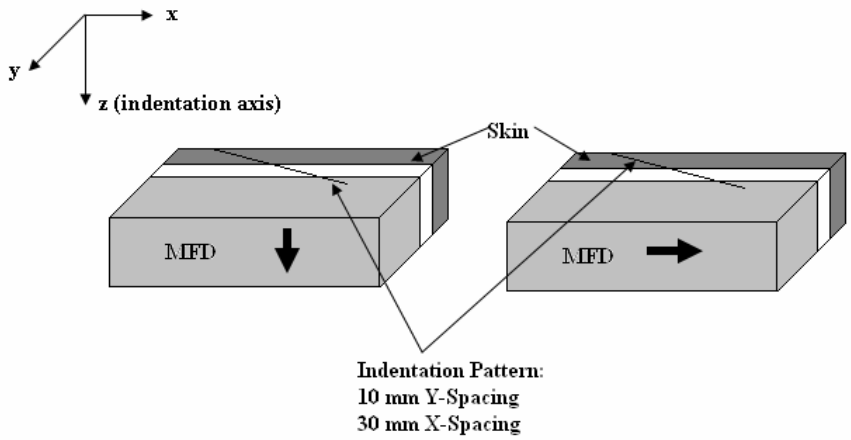

FIG 25. Schematic illustration of nanoindentation experiment setup.

Optical Microscopy

Cross-polarized optical microscopy was used to correctly identify the thickness of the morphological layers present in the neat PP system. Thick sections (~100 μm) were cut at room temperature using an Ultracut E microtome equipped with a cryoknife (Microstar). A drop of immersion oil was placed on a glass slide and the section was placed in the oil with a cover glass on top. The sections were viewed on an Olympus BX-60 optical microscope in transmission cross-polarized mode where the sample stage was rotated to obtain the point of maximum extinction. Images were captured using a camera and FPG image capture software.

Results and Discussion

Scratch Visibility Evaluation

From Figures 26 and 27, it is clear that there is indeed some surface anisotropy in the neat system as far as scratch visibility is concerned. Furthermore, the addition of erucamide not only dramatically increases the critical load for the onset of scratch visibility, it seems to be able to greatly reduce the anisotropic behavior, as the difference between the critical load values for the system containing erucamide is much smaller than that for the neat system.

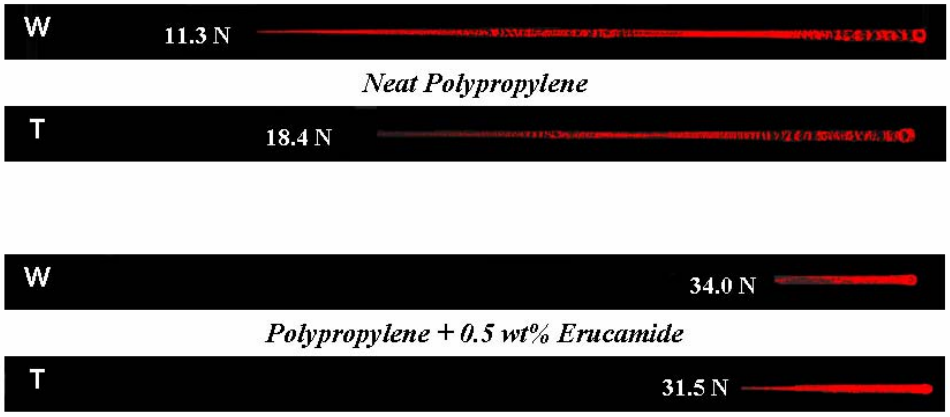

FIG 26. Scanned images of scratched surfaces of studied systems after processing with ImageJ. W = with flow, T = transverse to flow.

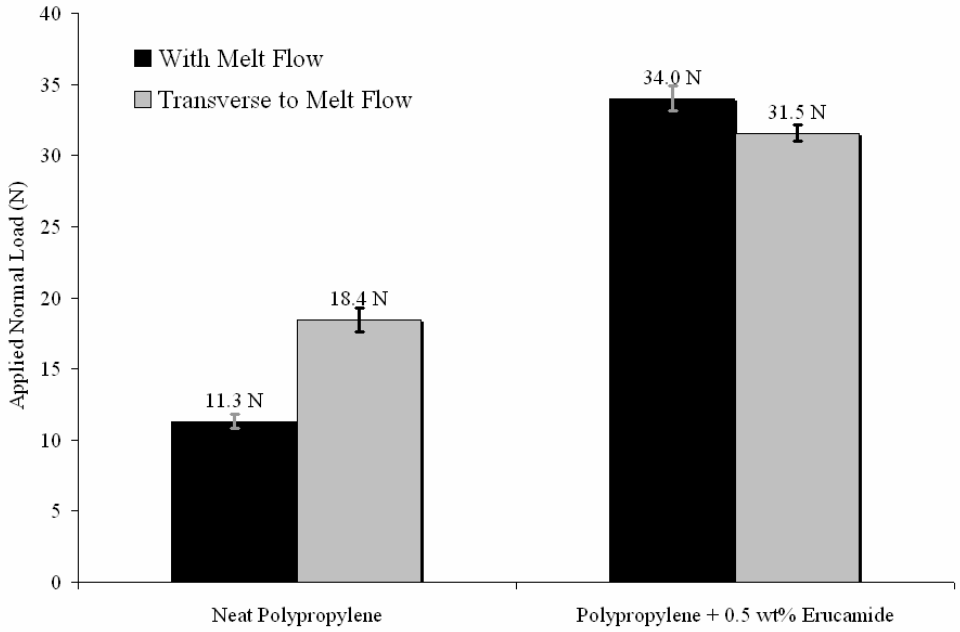

FIG 27. Critical load for the onset of scratch visibility for studied systems.

Surface Damage Morphology

As illustrated with previous examples, the appearance of the damage features that result in scratch visibility are just as important as where they occur. From the micrographs in Figure 28, it can be concluded that there is not a large difference in the appearance of the damage mechanisms when one compares the orientation, regardless of the system. However, for the neat system, it is counterintuitive that the damage mechanisms appear similar, but occur at different loads. This point will be further discussed later. For the system containing erucamide, the fact that the damage features are similar supports the claim that the incorporation of erucamide can overcome the effects of anisotropy.

Conversely, if the damage for the two model systems is compared, a difference can be seen. In the neat system, two transitions are observed. The damage starts out as the subtle, "fish-scale" type feature observed earlier. As the load increases, the material shows signs of ductile drawing and ironing, but in a chaotic, almost tearing manner until finally the material is, in fact, torn away and displaced. In the erucamide-containing system, only one transition was observed within this load range. In contrast to the neat system, this transition is much more sudden and seems to exhibit a more ordered pattern of ductile drawing and ironing. This is more than likely due to the minimization of the friction between the indenter and the PP surface.

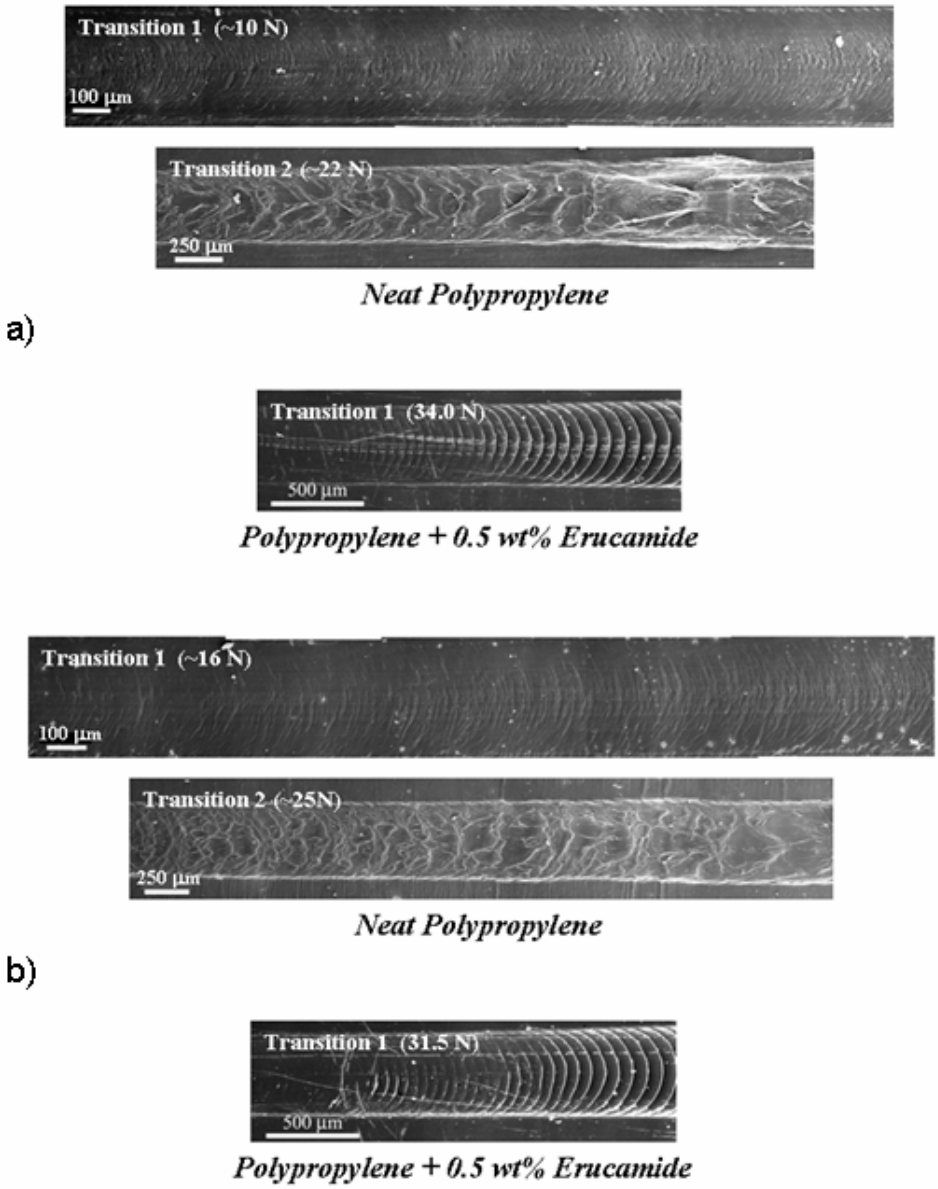

FIG 28. SEM micrographs of surface scratch morphology of studied polypropylene systems for scratch orientation a) with melt flow direction and b) transverse to melt flow direction.

Influence of Surface Friction

The reduction in the surface friction by the presence of erucamide can be observed by comparing the SCOF curves in Figure 29. The high level of friction between the sliding indenter and the non-lubricated material could play a role in the early onset of the micromechanisms that cause visible damage such as crazing, voiding, microcracking, as well as ductile drawing and ironing. Lubrication of the surface, while allowing for easier translation of the scratch tip, also greatly reduces the local stresses which would ultimately result in higher scratch resistance [43]. This reduction in the local stresses could also explain why the difference in the critical load for scratch visibility is not as great in the lubricated system versus the neat system.

Judging from the magnitude of the erucamide reference peak (1645 cm^{-1}) relative to that of the PP reference peak (1460 cm^{-1}) in the FTIR-ATR spectrum of the erucamide-containing PP system shown in Figure 30, it can be safely assumed that a great deal of the erucamide safely migrated to the surface of the PP. Such a distinct presence of surface lubricant would certainly greatly affect the frictional behavior of any material and this is reflected by the curves in Figure 29.

Spectroscopic Characterization of Anisotropy

As discussed above, IR dichroism is an effective way to quantify molecular orientation in polymers. After the two spectra were obtained, the peak at 973 cm^{-1} was used as the peak of interest (Figure 31). This peak represents backbone C-C stretching and rocking of the CH_2, CH_3 side groups in the amorphous phase [76]. An amorphous

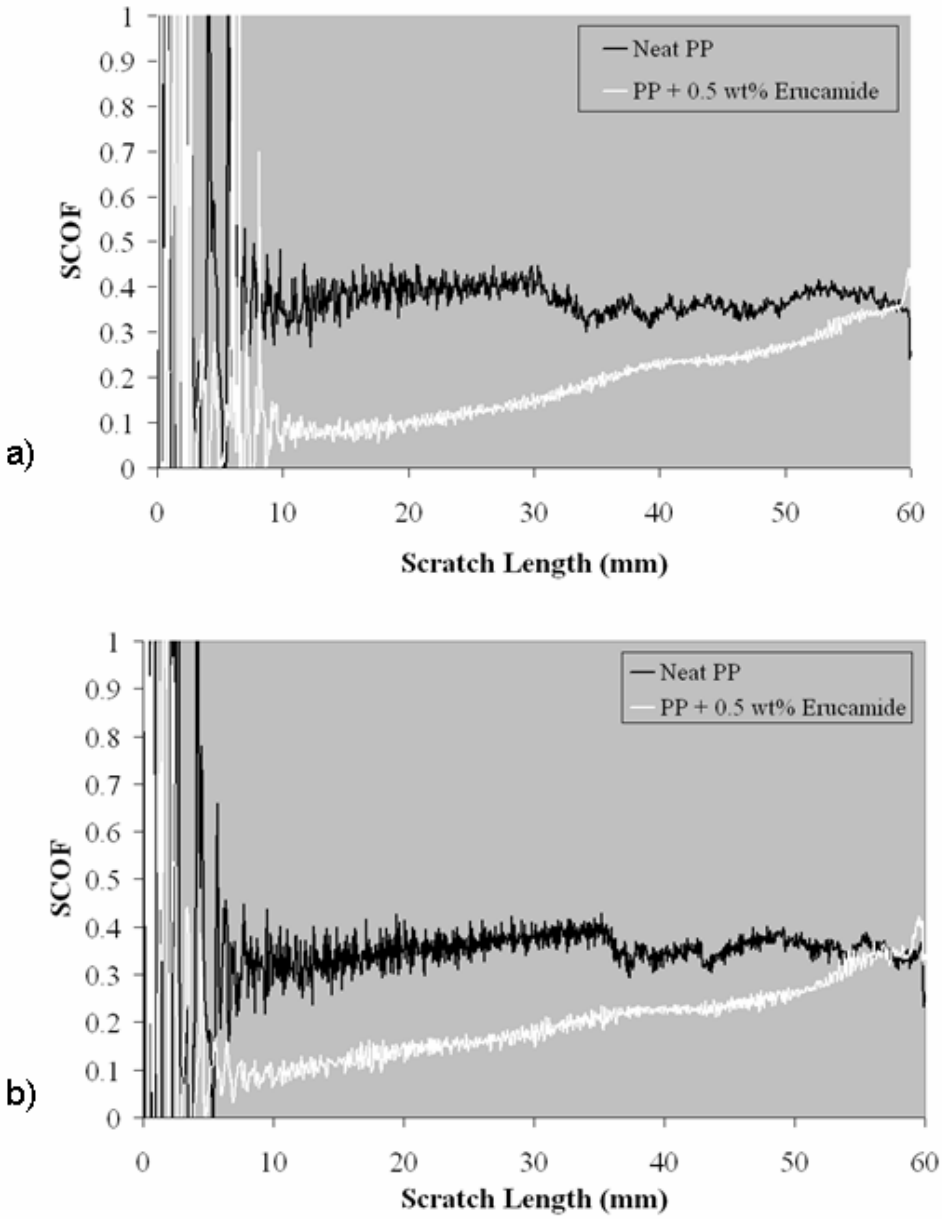

FIG 29. SCOF curves of studied polypropylene systems for scratch orientation a) with melt flow direction and b) transverse to melt flow direction.

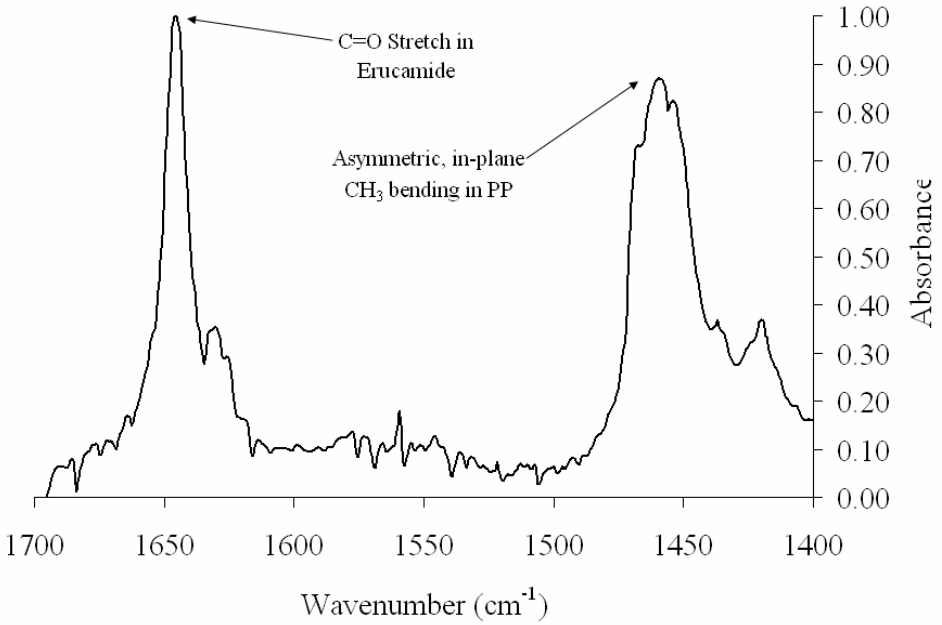

FIG 30. FTIR-ATR spectrum of polypropylene system containing 0.5 wt% erucamide.

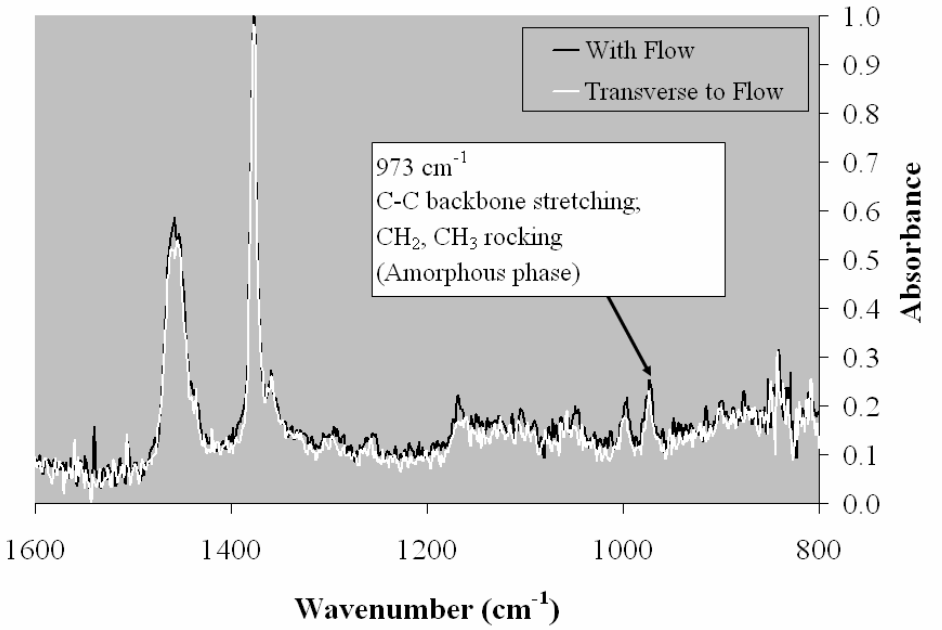

FIG 31. Spectra obtained for the neat polypropylene system with FTIR-ATR equipped with a ZnSe polarizer.

phase peak was chosen due to the fact that the skin will be highly amorphous since it is required to cool so quickly.

The dichroic ratio, *D*, was taken as the absorbance of the 973 cm-1 peak in the sample where the MFD was oriented in the direction of the laser path divided by the absorbance of the same peak when the sample's MFD was oriented perpendicular to the laser path. The orientation function was then calculated as follows:

$$f = \left[\frac{(D-1)}{(D+2)}\right]\left[\frac{(D_0+2)}{(D_0-1)}\right] \tag{4}$$

where D_0 is the dichroic ratio for an ideal uniaxially oriented specimen. D_0 can be calculated using Equation 5:

$$D_0 = 2 \cdot \cot^2(\alpha) \tag{5}$$

where α is the angle in radians between the vibrational transition moment and the chain axis, which for 973 cm^{-1} was calculated by Samuels to be 0.314 radians (18^o) [Reference]. The level of orientation can be judged by the value of *f*:

- f = -0.5 for orientation transverse to the MFD
- f = 0 for totally random orientation
- f = 1 for orientation parallel to the MFD

After performing the experiment on the neat PP system of this study, the value of *f* obtained was 0.033349. This value indicates that the chains are mainly randomly oriented, but that they are also oriented slightly with the flow direction. This can be possibly attributed to a non-uniform flow phenomenon known as "fountain-flow". The instant the molten polymer touches the cold mold walls, the polymer begins to cool

rapidly, preserving whatever orientation the chains were in at that instant. But as molding continues, the polymer is forced to flow, experiencing a complex stress state which forces the molten material to be pushed out from the center towards the walls. As a result, the polymer will have largely retained its random orientation, but since the molten polymer was flowing, the slight orientation in that direction might have also been preserved.

Nanomechanical Properties of Skin Layer

Figure 32 shows the different layers that comprise the skin/core morphology. The skin layer can be seen as the dark colored layer that starts at the sample surface and extends down into the bulk for a thickness of around 120 μm. The bright layer just beneath the skin is the transition layer. This layer is sandwiched between the skin layer and the core. Under the flow conditions, the transition layer is subjected to shear stress as it cools because it remains stationary near the skin, but is forced to flow near the molten core. This shear stress is what creates the high level of birefringence which contrasts with that in the skin layer. The next layer is the core layer where the polymer melt cools the slowest. This allows crystalline spherulites to form which are well-known to exhibit birefringence.

The curves in Figures 33 and 34 represent the results of the nanoindentation work done on the cross-sections of the neat PP bulk. These curves show that, although subtle, there is some difference between the mechanical properties of the skin layer for the two orientations. Although the overall differences between the curves is not

substantial enough to make any definitive claims regarding the orientation effect, the trend in the curves provides support for the claim that the skin indeed possesses anisotropic properties.

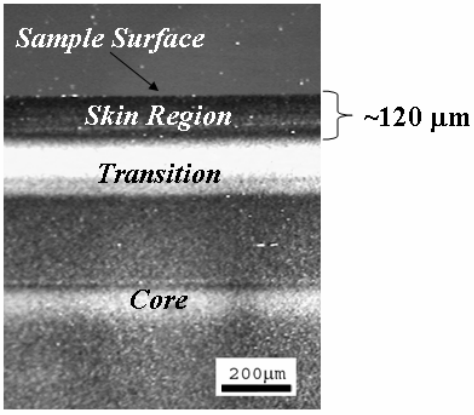

FIG 32. Optical microscope image of neat polypropylene viewed under cross-polars in transmission mode.

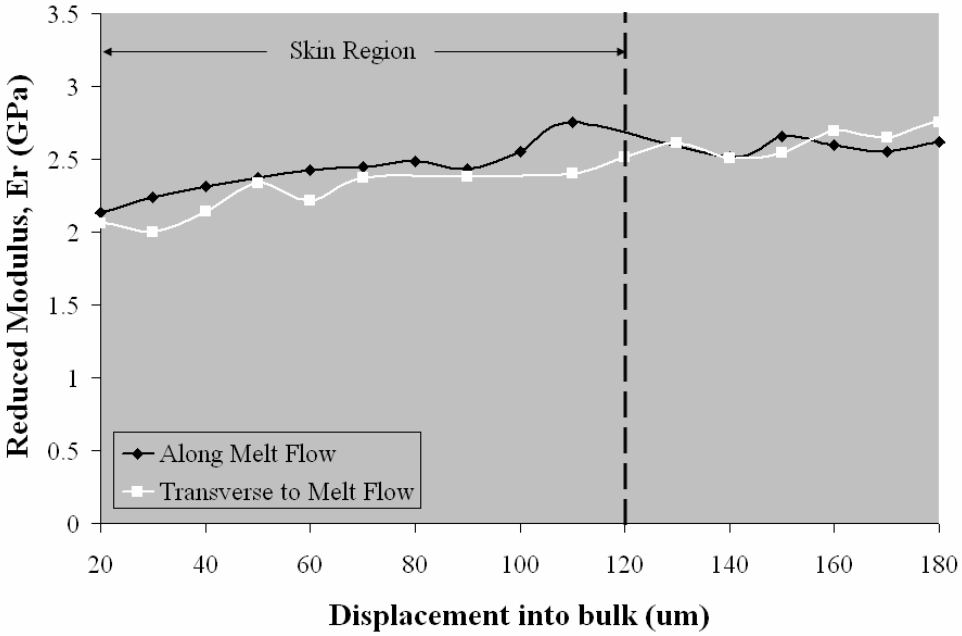

FIG 33. Reduced modulus as a function of the displacement of the indenter into the skin layer from the top surface.

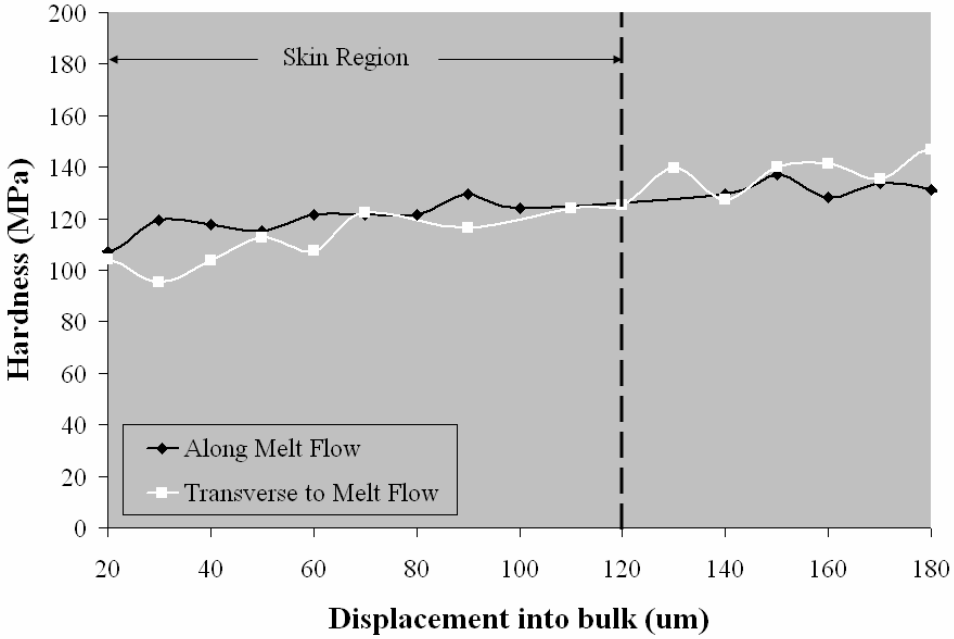

FIG 34. Indentation hardness as a function of the displacement of the indenter into the skin layer from the top surface.

CHAPTER V

CONCLUSIONS

The present body of work has focused on showing the effectiveness of the application of a recently standardized testing and analysis method to polymer materials. The scratch behavior analysis, when coupled with analysis using material science tools, provides meaningful information that can be used to engineer high-performance polymers with good scratch resistance.

In the case of polymer coatings, current testing methods do not seem adequate for fully addressing the fundamental issues regarding scratch behavior. However, by directly applying the standardized scratch test method, important information can be gleaned. When the ductility of the coating is considered, it appears that a ductile coating, overall, will experience less damage than a brittle coating, especially local adhesive delamination. From the thickness aspect, it is suggested that as thickness increases, the dependence of the severity of the scratch damage on the thickness decreases.

The scratch behavior of talc-reinforced thermoplastic olefins was also investigated. When erucamide is incorporated into the matrix, the level of surface lubrication provided greatly improves the scratch performance. Additionally, the level of surface treatment of the talc additive has a distinct effect on the ability of the erucamide to migrate to the surface. It is speculated that the untreated talc filler has either a physical or chemical propensity to adsorb the erucamide onto its surface, thus

trapping it inside the matrix and providing little facial lubrication. Special surface treatment of the talc seems to not only maximize the ability of the erucamide to reach the surface, but it also reduces the loading requirement of erucamide. This is reflected in the fact that using half the amount (by weight) of erucamide with surface treated talc than that used with untreated talc results in an increase of almost 7 Newtons in the critical load for the onset of scratch visibility.

For a more fundamental study, the scratch test was applied to polypropylene to investigate the surface anisotropy introduced by injection molding. From the visibility analysis alone, it is plainly evident that polymers are more vulnerable to visible damage when the scratch is oriented in the melt flow direction as opposed to transverse to the melt flow. The level of anisotropy was quantified using FTIR dichroism. It was found that the molecules at the surface of the polypropylene are randomly oriented with a slight preference for orientation along the melt flow direction, possibly due to non-uniform flow conditions. The cause of the dissimilarity in scratch visibility is suspected to be because of frictional behavior. The inclusion of 0.5 wt% erucamide into the neat polypropylene matrix improves the scratch performance by dramatically lowering the SCOF while greatly increasing the critical load for onset of scratch visibility and also seems to do away with the anisotropic effect.

In conclusion, the scratch test method, now standardized under desitgnation ASTM D7027-05, has been shown to be robust in addressing a wide variety of scenarios important to polymer engineering and science in an objective and quantitative fashion. Now that the method has shown its capability, work should begin to address the more

fundamental issues that will lead to complete, all-encompassing understanding of polymer scratch behavior.

REFERENCES

1. ASTM D 7027-05, "Standard Test Method for Evaluation of Scratch Resistance of Polymeric Coatings and Plastics Using an Instrumented Scratch Machine," ASTM International (2005).
2. I. M. Hutchings, P. Z. Wang, and G. C. Parry, *Surface and Coatings Technology,* **165**, 186 (2003).
3. P. Rangarajan, M. Sinha, V. Watkins, K. Harding, and J. Sparks, *Polymer Engineering and Science,* **43**, 749 (2003).
4. R. S. Kody and D. C. Martin, *Polymer Engineering and Science,* **36**, 298 (1996).
5. B. J. Briscoe, P. D. Evans, E. Pelillo, and S. K. Sinha, *Wear,* **200**, 137 (1996).
6. P. Bertrand-Lambotte, J. L. Loubet, C. Verpy, and S. Pavan, *Thin Solid Films*, **398**, 306 (2001).
7. S. J. Bull, R. I. Davidson, K. Harvathova, D. Mitchell, and J. R. White, *Journal of Materials Science,* **37**, 4937 (2002).
8. R. L. De Rosa and S. R. Wagner, *Journal of Adhesion,* **78**, 113 (2002).
9. C. Flosbach and W. Schubert, *Progress in Organic Coatings,* **43**, 123 (2001).
10. I. S. Goldstein and R. DeLong, *Journal of Vacuum Science and Technology,* **20**, 327 (1981).
11. L. Lin, G. S. Blackman, and R. R. Matheson, *Progress in Organic Coatings,* **40**, 85 (2000).

12. U. Schulz, V. Wachtendorf, T. Klimmasch, and P. Alers, *Progress in Organic Coatings,* **42**, 38 (2001).
13. ASTM D 6677, "Standard Test Method for Evaluating Adhesion by Knife," ASTM International (2001).
14. ASTM D 3359, "Standard Test Methods for Measuring Adhesion by Tape Test," ASTM International (1997).
15. ASTM D 3363, "Standard Test Method for Film Hardness by Pencil Test," ASTM International (2000).
16. ASTM D 4541, "Standard Test Method for Pull-Off Strength of Coatings Using Portable Adhesion Testers," ASTM International (1995).
17. ASTM D 2197, "Standard Test Method for Adhesion of Organic Coatings by Scrape Adhesion," ASTM International (1998).
18. ASTM ISO 1522, "Paints and Varnishes - Pendulum Damping Test," ASTM International (1998).
19. J. Chu, C. Xiang, H. J. Sue, and R. D. Hollis, *Polymer Engineering and Science,* **40**, 944 (2000).
20. J. S. S. Wong, H. J. Sue, K. Y. Zeng, R. K. Y. Li, and Y. W. Mai, *Acta Materialia,* **52**, 431 (2004).
21. M. Wong, G. T. Lim, A. Moyse, J. N. Reddy, and H. J. Sue, *Wear,* **256**, 1214 (2004).
22. M. Wong, A. Moyse, F. Lee, and H. J. Sue, *Journal of Materials Science,* **39**, 3293 (2004).

23. C. Xiang, H. J. Sue, J. Chu, and B. Coleman, *Journal of Polymer Science Part B-Polymer Physics,* **39**, 47 (2001).

24. C. Xiang, H. J. Sue, J. Chu, and K. Masuda, *Polymer Engineering and Science,* **41**, 23 (2001).

25. S. J. Bull, *Tribology International,* **30**, 491 (1997).

26. S. J. Bull and D. S. Rickerby, *Thin Solid Films,* **181**, 545 (1989).

27. S. J. Bull, D. S. Rickerby, A. Matthews, A. Leyland, A. R. Pace, and J. Valli, *Surface & Coatings Technology,* **36**, 503 (1988).

28. N. Frey, P. Mettraux, G. Zambelli, and D. Landolt, *Surface & Coatings Technology,* **63**, 167 (1994).

29. A. Hult, A. Krupicka, and M. Johansson, *Progress in Organic Coatings,* **46**, 32 (2003).

30. M. Laugier, *Thin Solid Films,* **76**, 289 (1981).

31. M. T. Laugier, *Thin Solid Films,* **117**, 243 (1984).

32. J. C. M. Li, *Materials Science and Engineering A,* **317**, 197 (2001).

33. L. Lin, G. S. Blackman, and R. R. Matheson, *Materials Science and Engineering A,* **317**, 163 (2001).

34. H. Ollendorf and D. Schneider, *Surface and Coatings Technology,* **113**, 86 (1999).

35. A. J. Perry, *Thin Solid Films,* **107**, 167 (1983).

36. P. Richard, J. Thomas, D. Landolt, and G. Gremaud, *Surface & Coatings Technology,* **91**, 83 (1997).

37. D. S. Rickerby, *Surface & Coatings Technology,* **36**, 541 (1988).

38. P. A. Steinmann, Y. Tardy, and H. E. Hintermann, *Thin Solid Films,* **154**, 333 (1987).

39. J. L. Bucaille, E. Felder, and G. Hochstetter, *Wear,* **249**, 422 (2001).

40. J. L. Bucaille, E. Felder, and G. Hochstetter, *Journal of Tribology,* **126**, 372 (2004).

41. S. J. Bull and D. S. Rickerby, *Surface & Coatings Technology,* **42**, 149 (1990).

42. I. Demirci, C. Gauthier, and R. Schirrer, *Thin Solid Films,* **479**, 207 (2005).

43. H. Jiang, G. T. Lim, J. N. Reddy, J. D. Whitcomb, and H. J. Sue, *Journal of Polymer Science - Polymer Physics Edition*, (Submitted December 2005).

44. G. T. Lim, "FEM Modeling of Scratch Behavior of Polymers", Ph.D. Dissertation, Texas A&M University, (2004).

45. M. Urban, ed., *Stimuli-Responsive Polymeric Films and Coatings (ACS Symposium Series 912)*, Oxford University Press and American Chemical Society, Washington, D.C.**,** 166 (2005).

46. G. T. Lim, M. H. Wong, J. N. Reddy, and H. J. Sue, *JCT Research,* **2**, 361 (2005).

47. Y. C. Lu and D. M. Shinozaki, *Materials Science and Engineering A,* **396**, 77 (2005).

48. A. Rodrigo and H. Ichimura, *Surface and Coatings Technology,* **148**, 8 (2001).

49. Y. Xie and H. M. Hawthorne, *Surface and Coatings Technology,* **141**, 15 (2001).

50. Y. Xie and H. M. Hawthorne, *Surface and Coatings Technology,* **155**, 121 (2002).

51. P. J. Burnett and D. S. Rickerby, *Thin Solid Films,* **154**, 403 (1987).

52. P. J. Burnett and D. S. Rickerby, *Thin Solid Films,* **157**, 233 (1988).

53. V. Jardret and P. Morel, *Progress in Organic Coatings,* **48**, 322 (2003).

54. A. Krupicka, M. Johansson, O. Wanstrand, and A. Hult, *Progress in Organic Coatings,* **48**, 1 (2003).

55. S. Wirasate and F. J. Boerio, *Journal of Adhesion,* **81**, 509 (2005).

56. J. Chu, L. Rumao, and B. Coleman, *Polymer Engineering and Science,* **38**, 1906 (1998).

57. R. Hadal, A. Dasari, J. Rohrmann, and R. D. K. Misra, *Materials Science and Engineering a-Structural Materials Properties Microstructure and Processing,* **380**, 326 (2004).

58. H. Tang, "Near-Surface Deformation of Polypropylene Blends", Ph.D. Dissertation, University of Michigan, (2000).

59. J. Edenbaum,ed., *Plastics Additives and Modifiers Handbook*, Chapman and Hall, New York, 107 & 865 (1996).

60. N. B. Joshi and D. E. Hirt, *Applied Spectroscopy,* **53**, 11 (1999).

61. M. X. Ramirez, K. B. Walters, and D. E. Hirt, *Journal of Vinyl & Additive Technology,* **11**, 9 (2005).

62. A. S. Rawls, D. E. Hirt, M. R. Havens, and W. P. Roberts, *Journal of Vinyl & Additive Technology,* **8**, 130 (2002).

63. C. A. Shuler, A. V. Janorkar, and D. E. Hirt, *Polymer Engineering and Science,* **44**, 2247 (2004).

64. R. Gachter and H. Muller,ed., *Plastics Additives Handbook, 4th ed.*, Hanser Publishers, 423 (1993).

65. C. Brun, M. Fromm, F. Berger, P. Delobelle, J. Takadoum, E. Beche, A. Chambaudet, and F. Jaffiol, *Journal of Polymer Science Part B-Polymer Physics,* **41**, 1183 (2003).

66. K. H. Kim, A. I. Isayev, K. Kwon, and C. van Sweden, *Polymer,* **46**, 4183 (2005).

67. G. Kumaraswamy, R. K. Verma, A. M. Issaian, P. Wang, J. A. Kornfield, F. Yeh, B. S. Hsiao, and R. H. Olley, *Polymer,* **41**, 8931 (2000).

68. M. Moffitt, Y. Rharbi, W. Chen, J. D. Tong, M. A. Winnik, D. W. Thurman, J. P. Oberhauser, J. A. Kornfield, and R. A. Ryntz, *Journal of Polymer Science Part B-Polymer Physics,* **40**, 2842 (2002).

69. B. A. G. Schrauwen, L. C. A. Von Breemen, A. B. Spoelstra, L. E. Govaert, G. W. M. Peters, and H. E. H. Meijer, *Macromolecules,* **37**, 8618 (2004).

70. J. C. Viana, A. M. Cunha, and N. Billon, *Polymer,* **43**, 4185 (2002).

71. J. Karger-Kocsis, ed., *Polypropylene Structure, Blends and Composites, Volume 1: Structure and Morphology*, Chapman and Hall, New York, 168 (1995).

72. E. P. Moore, ed., *Polypropylene Handbook*, Hanser Publishers, New York, 165 (1996).

73. R. J. Samuels, *Journal of Polymer Science Part a-General Papers,* **3**, 1741 (1965).

74. R. J. Samuels, *Macromolecular Chemistry and Physics-Makromolekulare Chemie*, **Supplement 4**, 241 (1981).

75. J. J. Strebel, F. Mirabella, C. Blythe, and T. Pham, *Polymer Engineering and Science,* **44**, 1588 (2004).

76. G. R. Hofmann, M. S. Sevegney, and R. M. Kannan, *International Journal of Polymer Analysis and Characterization,* **9**, 245 (2004).

VITA

Name:	Robert Lee Browning
Address:	Department of Mechanical Engineering, 3123 TAMU, College Station, TX 77843
Email Address:	B_Squared02@yahoo.com
Education:	B.S., Chemical Engineering, Texas A&M University, 2004 M.S., Mechanical Engineering, Texas A&M University, 2006